ACS OMEGA

http://pubs.acs.org/journal/acsodf

Article

Dual-Ligand Strategy Employing Rigid 2,5-Thiophenedicarboxylate and 1,10-Phenanthroline as Coligands for Solvothermal Synthesis of Eight Lanthanide(III) Coordination Polymers: Structural Diversity, DFT Study, and Exploration of the Luminescent Tb(III) Coordination Polymer as an Efficient Chemical Sensor for Nitroaromatic Compounds

Nargis Akhter Ashashi, Zaib ul Nisa, Richa Singhaal, Charanjeet Sen, Musheer Ahmad, Antonio Frontera, and Haq Nawaz Sheikh*

Cite This: *ACS Omega* 2022, 7, 41370−41391

Read Online

ACCESS | Metrics & More | Article Recommendations | Supporting Information

ABSTRACT: Lanthanide coordination polymers (Ln-CPs) are potential chemosensors when fabricated to depict a detectable change in optical properties on interaction with target analytes. This work investigates the interaction of nitroaromatic compounds with Ln-CPs leading to induced changes in fluorescence emission intensity, a crucial strategy to develop a selective and sensitive system for the sensing of nitroaromatics. Approaching toward this objective, solvothermal reactions of 2,5-thiophenedicarboxylic (2,5-TDC) acid, 1,10-phenanthroline (1,10-Phen), and $Ln(NO_3)_3{\cdot}xH_2O$ are carried out to assemble eight Ln(III) coordination polymers $[Ln_2(2,5\text{-}TDC)_3(1,10\text{-}Phen)_2(H_2O)_2]$ [Ln = Pr (**1**), Nd (**2**)], $\{[Tb(2,5\text{-}TDC)_{1.5}(1,10\text{-}Phen)(H_2O)]\cdot DMF\}$ (**3**), and $[Ln(2,5\text{-}TDC)_{1.5}(1,10\text{-}Phen)]{\cdot}xH_2O$ (Ln = Tb (**4**), Dy (**5**), Ho (**6**), Er (**7**), and Yb (**8**)); $x = 0$ for CP **4**, **5**, **6**, and **8** and $x = 1$ for CP **7** with two different space groups and dimensions. The as-synthesized polymers **1**−**8** are characterized by powder X-ray crystallography, infrared spectroscopy, and thermogravimetric analysis. The structure-corroborated density functional theory (DFT) studies are done on the selected CPs to investigate the interactions between different structural motifs of the assembled CPs. The luminescence properties of CP **4** are explored in detail and are found to be highly sensitive for the detection of *p*-nitrotoluene as indicated by the most intensive fluorescence quenching with the lowest limit of detection (0.88 ppm) and high quenching constant (4.3×10^4 M^{-1}). Other nitro compounds (viz., *o*-nitrobenzaldehyde, *m*-nitroaniline, picric acid, *m*-dinitrobenzene, *p*-nitrophenol, and *p*-nitroaniline) are also screened for potential sensing by CP **4**.

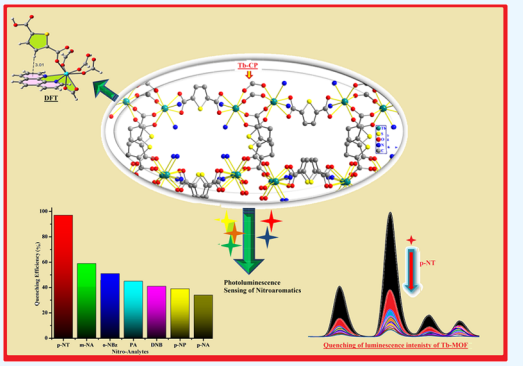

INTRODUCTION

Health and well-being of all living organisms, especially human beings, are of primary concern in today's scenario. Chemicals are essential ingredients of medicines, pesticides, dyes, explosives, papermaking, textile, and leather industries.[1] Among various chemicals used in our day-to-day life, nitroaromatic compounds and heavy metal ions are widely used,[2−6] which are extremely hazardous and lethal for life.[7,8] The explosiveness and deadly pollution caused by nitroaromatic compounds have concurrently raised worldwide concerns of public safety and environmental problems. Nitroaromatic compounds, such as *p*-nitrotoluene (*p*-NT), *o*-nitrobenzaldehyde, *m*-nitroaniline, picric acid, *m*-dinitrobenzene, *p*-nitrophenol, and *p*-nitroaniline, are potentially persistent and bioaccumulating and have high lethality, causing a great threat to the living things. Most of the nitroaromatics are mutagenic and carcinogenic, whereas some exhibit hematotoxic and hepatotoxic behaviors.[9−15] Therefore, the United States Environmental Protection Agency (USEPA) has designated nitroaromatics as "one of the priority pollutants". Consequently, reliable and efficient detection of nitroaromatic compounds is the need of the hour for environmental safety, humanitarian concerns, and national security.[16−18] Various physicochemical methodologies (viz., cyclic voltammetry, gas chromatography coupled with mass spectrometry, surface-enhanced Raman spectroscopy, ion mobility spectrometry, and

Received: August 12, 2022
Accepted: October 14, 2022
Published: October 31, 2022

Table 1. Summary of Crystal Data Ad Structure Refinement Parameters for CP 1−8

crystal data	CP 1	CP 2	CP 3	CP 4
empirical formula	$C_{42}H_{26}N_4O_{14}\ S_3Pr_2$	$C_{42}H_{26}N_4O_{14}S_3Nd_2$	$C_{25}H_{21}N_3O_8\ S_2Tb$	$C_{21}H_{11}N_2O_6S_2Tb$
CCDC	2181325	2181314	2181326	2181320
formula weight	1188.71	1195.33	1370.93	1188.71
crystal system, space group	triclinic, $\bar{P}1$	triclinic, $\bar{P}1$	triclinic, $\bar{P}1$	monoclinic, $C2/c$
temperature (K)	100	293	100 (2)	293
a, b, c (Å)	10.4969 (3), 11.1560 (3), 18.6618 (5)	10.5703 (1), 11.2032 (1), 18.6640 (1)	10.3911 (4), 11.1225 (5), 12.2861 (5)	24.8107 (2), 16.2859 (1), 11.9749 (1)
α, β, γ (deg)	106.039 (1), 91.507 (1), 94.710 (1)	106.478 (1), 91.214 (1), 94.683 (1)	78.2730 (10), 77.2540 (10), 65.6760 (10)	90, 93.356 (1), 90
V (Å^3)	2090.46 (10)	2110.09 (3)	1251.90 (9)	4830.34 (6)
Z	2	2	1	4
radiation type (λ = 0.71073)	Mo Kα	Mo Kα	Mo Kα	Mo Kα
μ (mm^{-1})	2.53	2.66	3.005	3.09
R_{int}	0.039	0.065	0.038	0.035
final R indexes [$I \geq 2\sigma(I)$]	R_1 = 0.0264, wR_2 = 0.0509	R_1 = 0.0202, wR_2 = 0.0494	R_1 = 0.0349, wR_2 = 0.0766	R_1 = 0.0203, wR_2 = 0.0469
final R indexes [all data]	R_1 = 0.0322, wR_2 = 0.0540	R_1 = 0.0221, wR_2 = 0.0504	R_1 = 0.0378, wR_2 = 0.0788	R_1 = 0.0229, wR_2 = 0.0481
largest diff. peak/hole (e/Å^3)	0.76/−0.64	0.73/−0.83	3.50/−2.16	0.96/−0.81
GOF on F^2	1.091	1.026	1.044	1.028
crystal data	CP 5	CP 6	CP 7	CP 8
empirical formula	$C_{21}H_{11}N_2O_6S_2Dy$	$C_{21}H_{11}N_2O_6S_2Ho$	$C_{21}H_{13}N_2O_7S_2Er$	$C_{21}H_{13}N_2O_6S_2Yb$
CCDC	2181321	2181322	2181323	2181324
formula weight	1195.85	1200.72	1241.40	1216.94
crystal system, space group	monoclinic, $C2/c$	monoclinic, $C2/c$	monoclinic, $C2/c$	monoclinic, $C2/c$
temperature (K)	293 (2)	293 (2)	296 (2)	296 (2)
a, b, c (Å)	24.8075 (3), 16.2806 (2), 11.9031 (10)	24.7446 (3), 16.26240 (19), 11.89081 (13)	24.4231 (4), 16.0851 (3), 12.0205 (2)	24.4139 (5), 16.1151 (3), 11.9290 (3)
α, β, γ (deg)	90, 93.195 (10), 90	90, 93.1825 (10), 90	90, 93.748 (2), 90	90, 93.595 (2), 90
V (Å^3)	4799.96 (9)	4777.57 (9)	4712.13 (14)	4684.02 (18)
Z	4	4	4	4
radiation type (λ = 0.71073)	Mo Kα	Mo Kα	Mo Kα	Mo Kα
μ (mm^{-1})	3.280	3.480	3.74	4.164
R_{int}	0.044	0.039	0.028	0.031
final R indexes [$I \geq 2\sigma(I)$]	R_1 = 0.0230, wR_2 = 0.0530	R_1 = 0.0211, wR_2 = 0.0487	R_1 = 0.0342, wR_2 = 0.0822	R_1 = 0.0374, wR_2 = 0.0963
final R indexes [all data]	R_1 = 0.0264, wR_2 = 0.0547	R_1 = 0.0237, wR_2 = 0.0497	R_1 = 0.0388, wR_2 = 0.0875	R_1 = 0.0418, wR_2 = 0.1015
largest diff. peak/hole (e/Å^3)	0.90/−0.81	0.98/−0.73	1.51/−2.33	2.37/−2.46
GOF on F^2	1.020	1.023	1.045	1.032

fluorescence)[19−27] have been adopted for the efficient sensing of nitroaromatics. Fluorescence quenching detection has attracted great interest owing to its high sensitivity, selectivity, reliability and short response time, although selective detection of nitroaromatics is still in its infancy. Therefore, it is necessary to develop effortless, speedy, and efficient experimental protocols for the detection of nitro compounds.

Crystal engineering of lanthanide(III)-organic hybrid materials has elicited considerable interest in the last two decades not only due to their diverse crystal structures and topologies[28−31] but also due to their potential as magnetoluminescent functional materials.[32−41] These materials are being developed as fluorescent chemical sensors particularly for various industrial/agricultural wastes in aqueous media.[42] All over the globe, different research groups have made efforts to synthesize functional coordination polymers (CPs) to establish new structure−property relationships.[43−45] Apart from purely structural issues, lanthanide(III) coordination polymers are widely explored as potential magnetoluminescent materials due to their inimitable properties arising from partially filled 4f electronic orbitals.[46−51]

The lanthanide(III) coordination polymers consisting of O- and N-heterocyclic linkers have been explored in detail (especially, furandicarboxylates[45,52−66] and pyridinedicarboxylates[67−72] are of special interest), but S-containing heterocycles, viz., di/polycarboxylic acids (especially based on thiophene-2,5-dicarboxylic acid; H_2TDC), are rarely explored.[73−76] Only a handful of coordination polymers/metal organic frameworks (MOFs) based on transition metals[77−80] and trivalent lanthanides[81−86] entangled with the 2,5-H_2TDC linker have been reported till date.

Numerous polar aprotic solvents such as *N*,*N*′-dimethylformamide (DMF), *N*,*N*′-dimethylacetamide (DMA), *N*,*N*′-diethylformamide (DEF), dimethyl sulfoxide (DMSO), and

https://doi.org/10.1021/acsomega.2c05179
ACS Omega 2022, 7, 41370−41391

Scheme 1. Bonding Modes Identified for Ligands Employed: 2,5-TDC^{2-} Linker (a−c) and 1,10-Phen (d)

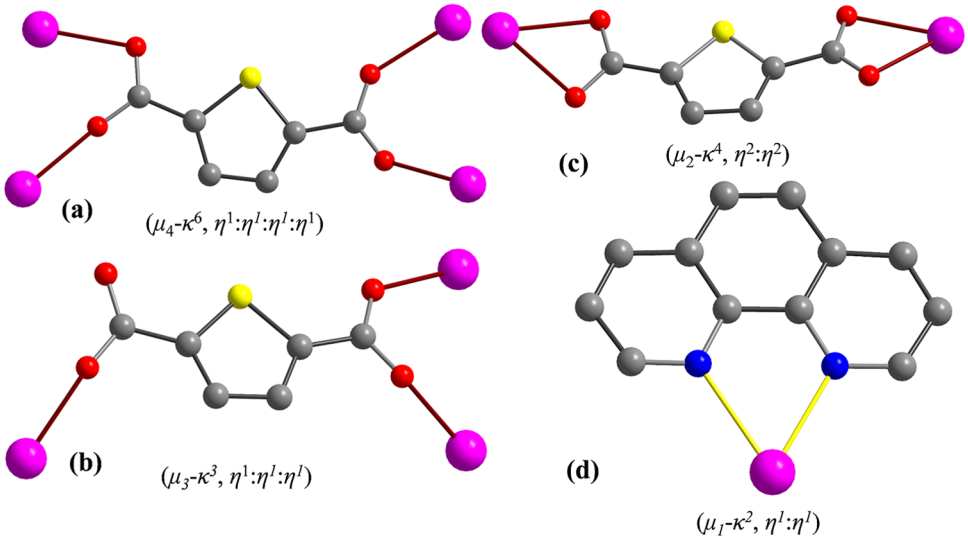

N-methyl-2-pyrrolidone (NMP or 1-methylpyrrolidin-2-one) having high boiling points have been extensively used for the self-assembly of coordination polymers/metal organic frameworks.[87,88] Among the aforementioned solvents, *N*,*N*′-dimethylacetamide (DMA) and dimethyl sulfoxide (DMSO) are the least explored.[89−93]

It is important to mention here that most of the reported CPs/MOFs with 2,5-H_2TDC have been designed without any auxiliary coligands.[73−76,81−86] To this end, we used 2,5-TDC as a linker and 1,10-Phen as a coligand to synthesize as much as eight highly related Ln(III)-CPs, namely, [Ln_2(2,5-TDC)$_3$(1,10-Phen)$_2$(H_2O)$_2$] [Ln = Pr (**1**), Nd (**2**)], {[Tb-(2,5-TDC)$_{1.5}$(1,10-Phen)(H_2O)]·DMF} (**3**), and [Ln(2,5-TDC)$_{1.5}$(1,10-Phen)]·*x*H_2O {Ln = Tb (**4**), Dy (**5**), Ho (**6**), Er (**7**), and Yb (**8**); *x* = 0 for CP **4**, **5**, **6**, and **8**, and *x* = 1 for CP **7** with two different space groups and dimensions} by employing a dual-ligand strategy. These CPs **1**−**8** have been prepared via a mixed-solvent strategy (DMA−H_2O, DMSO−water, and DMF−water systems).

Conceptually, the present work is constructed upon the experience acquired from studies on lanthanide(III) coordination polymers 2,5-thiophenedicarboxylates,[81,94] in which our research group explored the impact of polar aprotic solvents used (viz., DEF,[81] DMA[94]) and lanthanide contraction on the structures of CPs. Likewise, the assembled CPs **1**−**8** represent outstanding examples of tuning the crystal structures by the lanthanide contraction effect and solvent system used.

Various nitroaromatics (viz., *p*-nitrotoluene, *o*-nitrobenzaldehyde, *m*-nitroaniline, picric acid, *m*-dinitrobenzene, *p*-nitrophenol, and *p*-nitroaniline) were screened for potential luminescence sensing by CP **4** (Tb^{3+}). The present study elegantly reveals that CP **4** is a highly sensitive and promising luminescent probe for the detection of *p*-nitrotoluene (observed K_{sv} value for *p*-NT is 4.3 × 10^4 M^{-1} with a quenching efficiency of 97% at 100 ppm in aqueous media). To the best of our knowledge, this is the highest value of quenching constant reported for *p*-NT.

EXPERIMENTAL SECTION

Materials and Physical Measurements. Chemicals such as lanthanide(III) nitrates, 2,5-thiophenedicarboxylic acid (2,5-H_2TDC), 1,10-phenanthroline (1,10-Phen), *N*,*N*′-dimethylacetamide (DMA), and *N*,*N*′-dimethylformamide (DMF) used for the synthesis were analytical grade and were employed as such without further purification. A CHNS-932 Leco elemental analyzer was employed for C, H, N, and S microanalytical analysis of the synthesized CPs. Fourier transform infrared (FTIR) spectra for the synthesized CPs (4000−400 cm^{-1}) were recorded on a Shimadzu Prestige-21 Fourier transform infrared (FTIR) spectrophotometer by employing pressed KBr pellets. Powder X-ray diffraction (PXRD) studies were recorded to authenticate the phase purity of the prepared crystalline samples of CPs **1**−**8** on an Agilent Supernova X-ray diffractometer (Ni-filtered Cu Kα irradiation, λ = 0.1542 nm) at 45 kV and 40 mA, with the value of 2θ ranging between 5 and 50° (scan rate of 2°/min). Thermal stabilities of the synthesized CPs were investigated on a PerkinElmer (SGSA 6000) thermal analyzer, ranging from 30 to 950 °C with a heating rate of 10 °C/min. UV−visible (vis) spectra of CP **4**, ligands, and nitroaromatic compounds were recorded at room temperature using a PerkinElmer (Lambda 1050+) UV/Vis/near-infrared (NIR) spectrophotometer. The photoluminescence spectra of CP **4** were recorded using a Hitachi F-4700 fluorescence spectrophotometer with a xenon lamp as the excitation source.

Collection of Crystallographic Data and Structure Determination. Single-crystal X-ray diffractions (XRDs) were carried out to determine the crystal structures of CPs **1**−**8**. Single-crystal X-ray diffraction data were obtained on a SuperNova, single source at offset/far, HyPix3000 diffractometer by employing a graphite-monochromated Mo Kα (λ = 0.71073 Å) source. The crystals were kept at 293 (2), 296, and 100 (2) K during data collection. To solve the structure of the compounds, the Olex2[95] program was used with the ShelXT[96] structure solution program using intrinsic phasing and refined with the ShelXL[97] refinement package with least squares minimization on F^2. All the non-H atoms were refined anisotropically.[98−100] Using crystallographic data, TOPOS Pro[101] software was used to investigate the topology of the synthesized CPs. Diamond[102] and Mercury 3.8[103] programs were used for pictorial representation of the crystal structures of some selected CPs. Crystallographic data for the reported compounds have been deposited to the Cambridge Crystallographic Data Centre. CCDC: 2181325 (**1**; Pr), 2181314 (**2**;

https://doi.org/10.1021/acsomega.2c05179
ACS Omega 2022, 7, 41370−41391

Nd), 2181326 (**3**; Tb), 2181320 (**4**; Tb), 2181321 (**5**; Dy), 2181322 (**6**; Ho), 2181323 (**7**; Er), and 2181324 (**8**; Yb). The crystal data and structural refinement parameters for the synthesized CPs **1**−**8** are summarized in Table 1. The selected bond lengths and bond angles are tabulated in Tables S1−S16. The rigid 2,5-TDC linker exhibits three different coordination modes, namely tetradentate μ_4-κ^4, η^1:η^1:η^1:η^1, tridentate μ_3-κ^3, η^1:η^1:η^1:η^0, and tetradentate chelating μ_2-κ^4, η^1:η^1:η^1:η^1 (see Scheme 1a−c), while 1,10-phenanthroline exhibits only the bidentate chelating coordination mode μ_1-κ^2, η^1:η^1 (see Scheme 1d).

Fluorescence Spectral Detection. Photoluminescence sensing experiments for the detection of nitroaromatic compounds were performed on a fluorescence spectrophotometer at room temperature. A suspension of 10 mg of Tb^{3+}-based CP powder in 10 mL of H_2O was formed by sonicating for 30 min. This suspension was used as a probe for the detection of nitroaromatic compounds. Fluorescence measurements of the Tb^{3+}-based CP suspension were done by placing the suspension in a 5 mL quartz cuvette in a fluorescence spectrophotometer. Meanwhile, aqueous stock solutions of 100 ppm concentration (0.01 g of nitroanalyte in 100 mL of water) of nitro compounds were prepared. From all the prepared stock solutions, further 10 different diluted solutions with the concentration ranging from 10 to 100 ppm were prepared. Out of each prepared solution, 2.5 mL of the diluted nitroanalytes was added to 2.5 mL of CP **4** suspension taken in a 5 mL quartz cuvette. Then, the fluorescence spectrum was recorded immediately by exciting CP **4** at 252 nm. The slit widths of emission and excitation were maintained at 10 nm. Finally, the Stern−Volmer (S−V) equation $\{I_0/I = 1 + K_{sv}[M]\}$ was used to estimate the fluorescence quenching by different nitroanalytes.

Theoretical Methods. The calculations of the noncovalent interactions (NCIs) were carried out using Gaussian-16[104] and the PBE0-D3/def2-TZVP levels of theory.[105,106] To evaluate the interactions in the solid state, the crystallographic coordinates have been used and only the position of the H-atoms has been optimized. The interaction energies have been computed by calculating the difference between the energies of isolated monomers and their assembly. The interaction energies were calculated with correction for the basis set superposition error (BSSE) using the Boys−Bernardi counterpoise technique.[107] Bader's theory of "atoms in molecules" (QTAIM)[108] has been used to study the interactions discussed herein using the AIMAll calculation package.[109] The molecular electrostatic potential (MEP) surfaces have been computed using Gaussian-16 software.[104] To assess the nature of the interactions in terms of being attractive or repulsive, the NCIPLOT index was used, which is a method for plotting noncovalent interaction regions,[110] based on the noncovalent interaction (NCI) visualization index derived from the electronic density.[111] The reduced density gradient (RDG), coming from the density and its first derivative, is plotted as a function of the density (mapped as isosurfaces) over the molecule of interest. The sign of the second Hessian eigen value times the electron density [i.e., sign(λ_2)ρ in atomic units] enables the identification of attractive/stabilizing (blue green-colored isosurfaces) or repulsive (yellow red-colored isosurfaces) interactions using 3D plots.

Synthetic Protocols Used for the Synthesis of Ln-CPs 1−8. Single crystals suitable for single-crystal X-ray diffractions were prepared by a similar procedure for CPs **1**−**8**. Thus, the detailed synthetic procedure for CP **1** is given as follows.

*Synthesis of [Pr_2(2,5-TDC)$_3$(1,10-Phen)$_2$(H_2O)$_2$] (**1**).* To a suspension of 2,5-thiophenedicarboxylic acid (2,5-H_2TDC; 0.0172 g, 0.1 mmol) and 1,10-phenanthroline (1,10-Phen; 0.036 g, 0.2 mmol) in 4 mL of DMA, 6 mL of aqueous solution of $Pr(NO_3)_3{\cdot}6H_2O$ (0.017 g, 0.4 mmol) was added dropwise with continuous stirring on a magnetic stirrer. After stirring for about 30 min, the reaction mixture was transferred to a 23 mL Teflon-lined stainless-steel autoclave, sealed and heated under autogenous pressure at 160 °C for 24 h. After completion of the reaction, the explosive reaction mixture was gradually cooled to 25 °C at a rate of 5 °C/h. Light-green small-sized rhombus-shaped crystals were obtained with a yield of 49% based on Pr(III) ions. Anal. Calcd (%) for $C_{42}H_{26}N_4O_{14}S_3Pr_2$: C, 42.39; H, 2.18; N, 4.71; S, 8.09. Found (%): C, 42.06; H, 2.03; N, 4.61; S, 8.01. FTIR (KBr pellets, cm^{-1}): 3600(m), 3477(w), 3067(m), 2583(w), 2158(w), 1928(w), 1575(m), 1362(s), 1091(s), 763(s), 624(w), 463(s).

*Synthesis of [Nd_2(2,5-TDC)$_3$(1,10-Phen)$_2$(H_2O)$_2$] (**2**).* CP **2** was synthesized by a procedure similar to that of CP **1** with a stoichiometric equivalent of $Nd(NO_3)_3{\cdot}5H_2O$ (0.176 g, 0.4 mmol) used instead of $Pr(NO_3)_3{\cdot}6H_2O$. Light-purple rhombus-shaped crystals for CP **2** were obtained with a yield of 50% based on Nd(III) ions. Anal. Calcd (%) for $C_{42}H_{26}N_4O_{14}S_3Nd_2$: C, 42.16; H, 2.17; N, 4.68; S, 8.04. Found (%): C, 42.05; H, 2.03; N, 4.43; S, 8.00. FTIR (KBr pellets, cm^{-1}): 3501(w), 3059(m), 2600(w), 1633(s), 1526(s), 1310(s), 1099(m), 763(s), 624(m), 526(w), 460(s).

*Synthesis of {[Tb(2,5-TDC)$_{1.5}$(1,10-Phen)(H_2O)]·DMF} (**3**).* CP **3** was synthesized by a procedure similar to that of CP **1** with a stoichiometric equivalent of $Tb(NO_3)_3{\cdot}6H_2O$ (0.177 g, 0.4 mmol) used instead of $Pr(NO_3)_3{\cdot}6H_2O$ and solvent DMF used instead of DMA. Colorless rhombus-shaped crystals for CP **3** were obtained with a yield of 50% based on Tb(III) ions. Anal. Calcd (%) for $C_{24}H_{20}N_3O_8S_2Tb$: C, 42.00; H, 2.90; N, 5.81; S, 13.42. Found (%): C, 42.01; H, 2.94; N, 5.88; S, 13.47. FTIR (KBr pellets, cm^{-1}: 3503(m), 3089(w), 2933(m), 2586(w), 2162(w), 1528(s), 1371(s), 1266(m), 1135(m), 1035(m), 971(m), 780(s), 688(m), 595(m), 462(s).

*Synthesis of [Tb(2,5-TDC)$_{1.5}$(1,10-Phen)] (**4**).* CP **4** was synthesized by a procedure similar to that of CP **1** with a stoichiometric equivalent of $Tb(NO_3)_3{\cdot}6H_2O$ (0.177 g, 0.4 mmol) used instead of $Pr(NO_3)_3{\cdot}6H_2O$. Colorless rhombus-shaped crystals for CP **4** were obtained with a yield of 50% based on Tb(III) ions. Anal. Calcd (%) for $C_{21}H_{11}N_2O_6S_2Tb$: C, 41.33; H, 1.81; N, 4.5; S, 10.48. Found (%): C, 41.12; H, 1.43; N, 4.0; S, 10.26. FTIR (KBr pellets, cm^{-1}: 3501(w), 3059(m), 2600(w), 1633(s), 1526(s), 1310(s), 1099(m), 763(s), 624(m), 526(w), 460(s).

*Synthesis of [Dy(2,5-TDC)$_{1.5}$(1,10-Phen)] (**5**).* CP **5** was synthesized by a procedure similar to that of CP **1** with a stoichiometric equivalent of $Dy(NO_3)_3{\cdot}5H_2O$ (0.176 g, 0.4 mmol) used instead of $Pr(NO_3)_3{\cdot}6H_2O$. Colorless rhombus-shaped crystals for CP **5** were obtained with a yield of 51% based on Dy(III) ions. Anal. Calcd (%) for $C_{21}H_{11}N_2O_6S_2Dy$: C, 41.09; H, 1.80; N, 4.56; S, 10.43. Found (%): C, 41.0; H, 1.73; N, 4.18; S, 10.16. FTIR (KBr pellets, cm^{-1}): 3649(w), 3501(m), 3051(m), 2920(m), 2592(w), 1633(s), 1526(s), 1370(s), 1207(w), 1099(w), 1018(w), 838(m), 763(s), 665(m), 526(w), 468(s), 411(m).

*Synthesis of [Ho(2,5-TDC)$_{1.5}$(1,10-Phen)] (**6**).* CP **6** was synthesized by a procedure similar to that of CP **1** with a

https://doi.org/10.1021/acsomega.2c05179
ACS Omega 2022, 7, 41370−41391

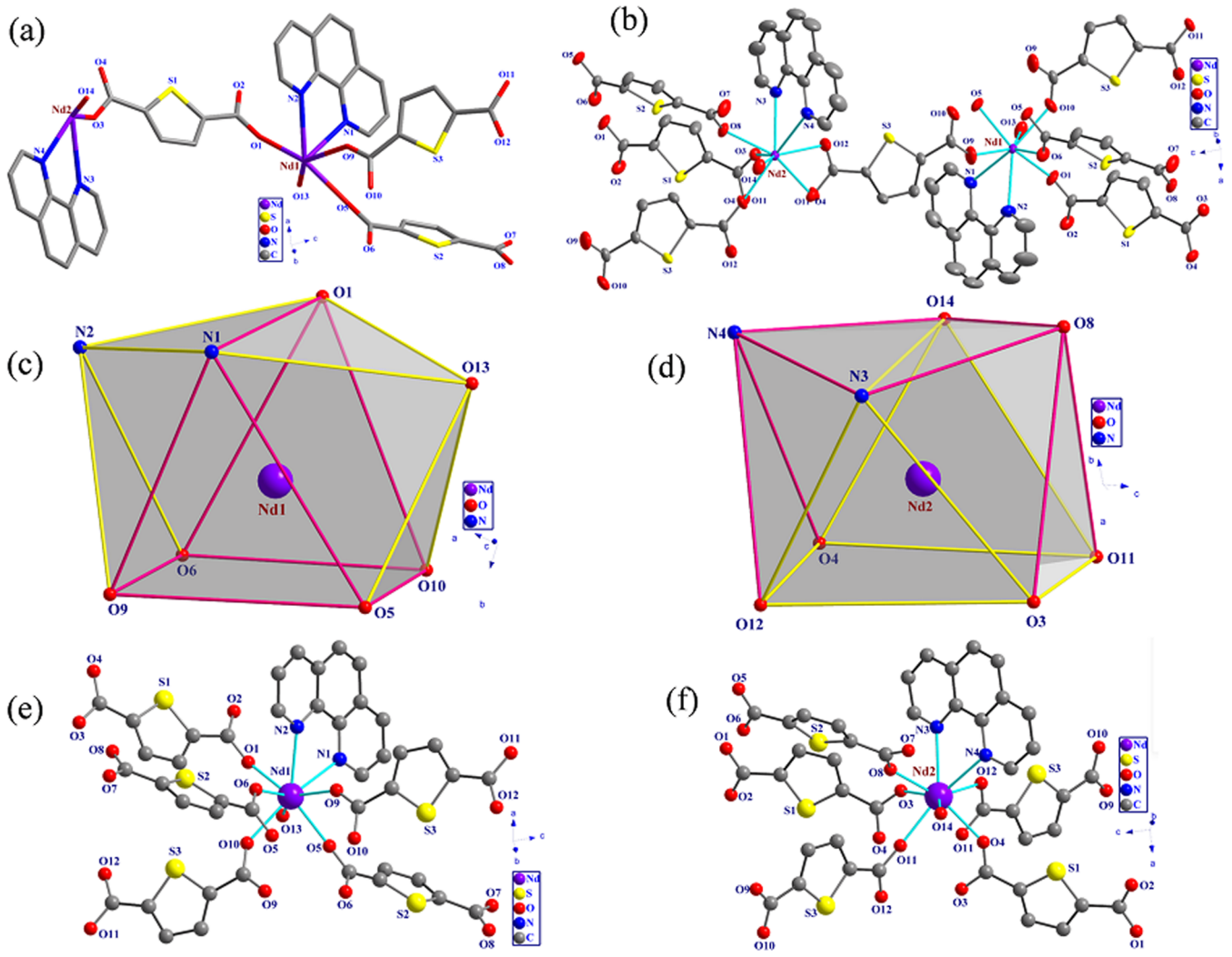

Figure 1. Pictographic representation of the crystal structure of CP **2**; (a) asymmetric unit for CP **2**; (b) ORTEP view of the structural unit (the thermal displacement ellipsoids are drawn at 50% probability; H atoms are omitted for structural clarity); (c) square antiprismatic polyhedral geometry around the Nd1 center; (d) bicapped trigonal prism polyhedral geometry around the Nd2 center; (e) coordination environment of Nd1; and (f) coordination environment of Nd2.

stoichiometric equivalent of $Ho(NO_3)_3{\cdot}5H_2O$ (0.176 g, 0.4 mmol) used instead of $Pr(NO_3)_3{\cdot}6H_2O$. Light-brown rhombus-shaped crystals were obtained with 54% yield based on Ho(III). Anal. Calcd (%) for $C_{21}H_{11}N_2O_6S_2Ho$: C, 40.92; H, 1.79; N, 4.54; S, 10.38. Found (%): C, 40.56; H, 1.71; N, 4.08; S, 10.08. FTIR (KBr pellets, cm^{-1}): 3468(m), 3059(m), 2920(m), 2592(w), 1936(w), 1633(s), 1526(s), 1378(s), 1198(w), 1099(m), 1010(w), 829(m), 772(s), 723(s), 682(m), 591(w), 460(s).

*Synthesis of [Er(2,5-TDC)$_{1.5}$(1,10-Phen)]·H$_2$O (**7**).* CP **7** was synthesized by a procedure similar to that of CP **1** with a stoichiometric equivalent of $Er(NO_3)_3{\cdot}5H_2O$ (0.176 g, 0.4 mmol) used instead of $Pr(NO_3)_3{\cdot}6H_2O$. Light-pink rhombus-shaped crystals were obtained with 50% yield based on Er(III). Anal. Calcd (%) for $C_{21}H_{13}N_2O_7S_2Er$: C, 39.62; H, 2.05; N, 4.40; S, 10.05. Found (%): C, 39.28; H, 1.44; N, 4.0; S, 10.01. FTIR (KBr pellets, cm^{-1}): 3657(w), 3485(m), 3051(m), 2920(m), 2592(w), 1911(w), 1633(s), 1526(s), 1378(s), 1215(w), 1099(m), 1018(m), 919(w), 838(m), 772(s), 674(m), 518(w), 468(s).

*Synthesis of [Yb(2,5-TDC)$_{1.5}$(1,10-Phen)] (**8**).* CP **8** was synthesized by a procedure similar to that of CP **1** with a stoichiometric equivalent of $Yb(NO_3)_3{\cdot}5H_2O$ (0.176 g, 0.4 mmol) used instead of $Pr(NO_3)_3{\cdot}6H_2O$. Colorless rhombus-shaped crystals were obtained with 52% yield based on Yb(III). Anal. Calcd (%) for $C_{21}H_{11}N_2O_6S_2Yb$: C, 40.39; H, 1.77; N, 4.48; S, 10.25. Found (%): C, 40.13; H, 1.34; N, 4.13; S, 10.18. FTIR (KBr pellets, cm^{-1}): 3657(w), 3501(m), 3051(m), 2583(w), 1936(w), 1649(s), 1526(s), 1370(s), 1215(w), 1091(w), 1010(m), 919(w), 843(s), 763(s), 674(m), 591(w), 468(s).

RESULTS AND DISCUSSION

Synthetic Analysis. Eight new coordination polymers (CPs **1**−**8**) were procured under solvothermal synthesis by employing DMA−water and DMF−water (ratio 1:2) as the solvent systems by taking 2,5-thiophenedicarboxylic acid (2,5-H_2TDC) and 1,10-phenanthroline (1,10-Phen) as rigid ligands with $Ln(NO_3)_3{\cdot}nH_2O$, [Ln = Pr (**1**), Nd (**2**), Tb (**3**, **4**), Dy (**5**), Ho (**6**), Er (**7**), and Yb (**8**)]. To optimize the reaction conditions, we tried the variable conditions of temperature, different ratios of the solvent, metal-to-ligand proportions, and reaction heating period. The CPs **1**−**8** are stable toward exposure to air and moisture and almost insoluble in common

https://doi.org/10.1021/acsomega.2c05179
ACS Omega 2022, 7, 41370−41391

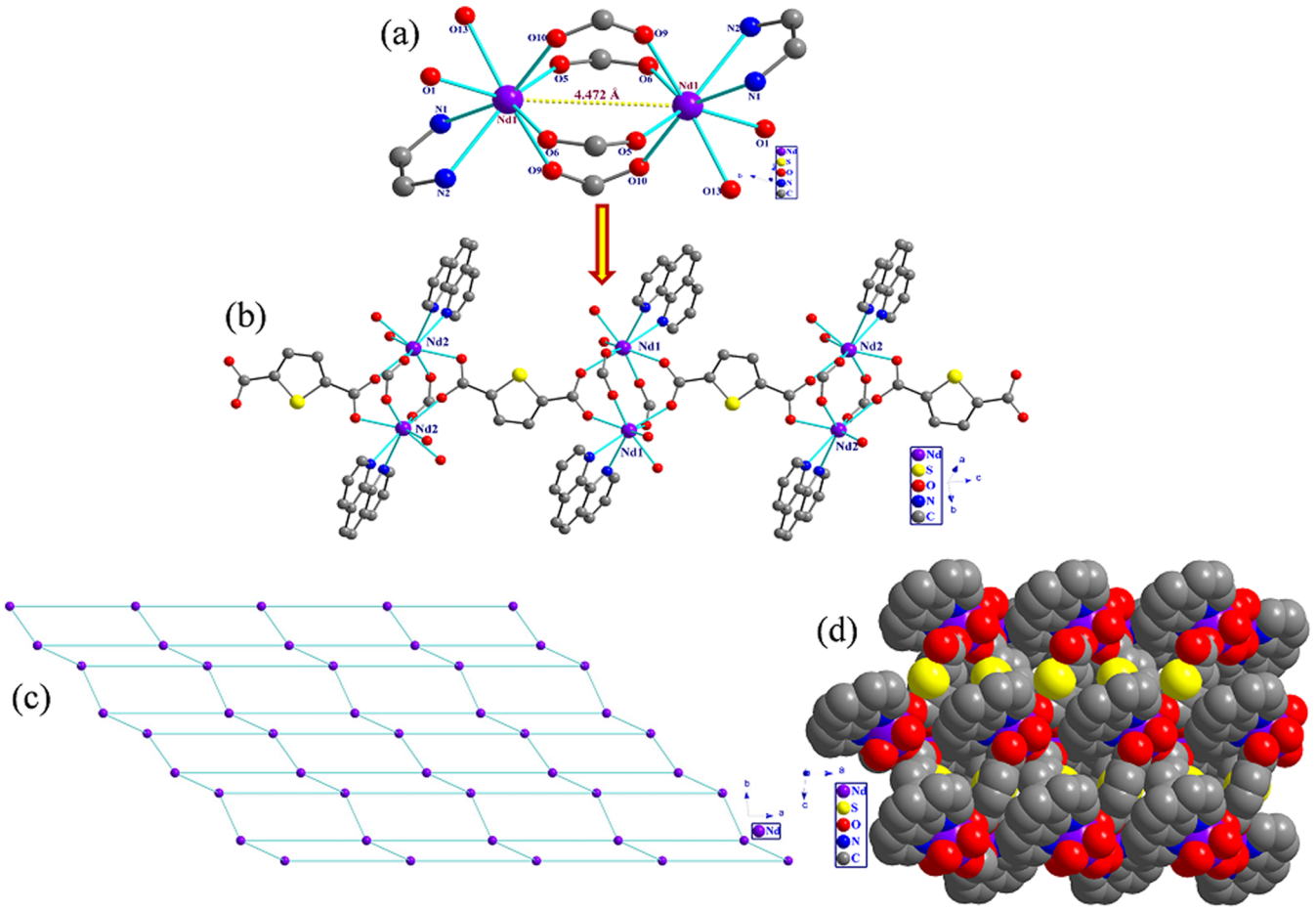

Figure 2. (a) Tetranuclear SBU $[Nd_4O_{24}N_4]$ identified for CP **2**. (b) 1D extension of tetranuclear SBU $[Nd_4O_{24}N_4]$ for CP **2**. (c) Topological view along the *c*-axis and (d) space-filling model along the *b*-axis of CP **2**.

solvents such as water, dimethylformamide, dimethylacetamide, dimethyl sulfoxide, ethanol, methanol, acetonitrile, etc.

*Structural Description of {[Ln$_2$(2,5-TDC)$_3$(1,10-Phen)$_2$(H$_2$O)$_2$]}$_n$ {Ln = Pr (**1**) and Nd (**2**)}.* X-ray crystallographic studies depict that the synthesized CPs **1** and **2** are isomorphous and crystallize in the centrosymmetric $P\bar{1}$ space group of the triclinic crystal system, forming a two-dimensional (2D) polymeric structure with the unit cell volume ranging from 2090.46 (10) to 2110.09 (3) Å; see Table 1. Both the CPs are isostructural and depict similar coordination geometry. Therefore, herein, we discuss the detailed structural features of CP **2** (Nd) as a representative example. The asymmetric unit of CP **2** has two crystallographically independent Nd(III) ions, three fully deprotonated 2,5-TDC^{2-} units, and two 1,10-Phen and coordinated water molecules each. In the asymmetric unit, Nd1 is surrounded by two nitrogen atoms N1 and N2 from one 1,10-Phen moiety and four oxygen atoms, viz., O1, O5, O7, and O13, out of which O1, O5, and O7 originate from three distinct 2,5-TDC^{2-} molecules, whereas O13 stems from one coordinated water molecule. On the other hand, Nd2 is surrounded by two nitrogen atoms N3 and N4 from one 1,10-Phen moiety and two oxygen atoms O3 and O14 originating from one 2,5-TDC^{2-} moiety and one coordinated water molecule, respectively (see Figure 1a).

The rigid 2, 5-TDC^{2-} moiety features two different bonding modes, which are tetradentate μ_4-κ^4, η^1:η^1:η^1:η^1 and tridentate μ_3-κ^3, η^1:η^1:η^1:η^0, as portrayed in Scheme 1a,b, while the other rigid 1,10-Phen exhibits only one bidentate chelating μ_1-κ^2, η^1:η^1 coordination mode (see Scheme 1d). The ORTEP view of CP **2** at 50% probability of thermal ellipsoids is represented in Figure 1b. The H atoms are omitted for clarity of the crystal structure. In CP **2**, Nd1 and Nd2, both with a coordination number of eight, are surrounded by the $[O_6N_2]$ donor set (see Figure 1c,d). As shown in Figure 1e,f, the coordination environments of both Nd1 and Nd2 are surrounded by one bidentate chelating 1,10-phenanthroline unit, five 2,5-thiophenedicarboxylate linkers, and one coordinated water molecule. In the coordination environment of Nd1, five oxygen atoms, viz., O1, O5, O6, O9, and O10, originate from five unidentate carboxylate groups of five distinct 2,5-TDC^{2-}, two nitrogen atoms, viz., N1 and N2 stem from one 1,10-phenanthroline unit, and one oxygen atom O13 belongs to the coordinated water molecule (see Figure 1e).

Similarly, the coordination environment of Nd2 consists of five oxygen atoms viz., O3, O4, O8, O11, and O12, originating from five carboxylate groups of five distinct 2,5-TDC^{2-}, two nitrogen atoms, viz., N3 and N4 stemming from one 1,10-phenanthroline, and one oxygen atom O14 stemming from the coordinated water molecule (see Figure 1f).

The crystal structure of CP **2** (Nd) unveils a tetranuclear $[Nd_4O_{24}N_4]$ secondary building unit (SBU) (see Figure 2a). Two symmetrically distinct eight-coordinated metal centers possess two different polyhedral geometries, i.e., square antiprismatic (D_{4d}) around Nd1 and bicapped trigonal prism (D_{3h}) around Nd2.[112] The tetranuclear $[Nd_4O_{24}N_4]$ SBU in CP **2** consists of two subunits $[Nd_2O_{12}N_2]$ with Nd···Nd

https://doi.org/10.1021/acsomega.2c05179
ACS Omega 2022, 7, 41370−41391

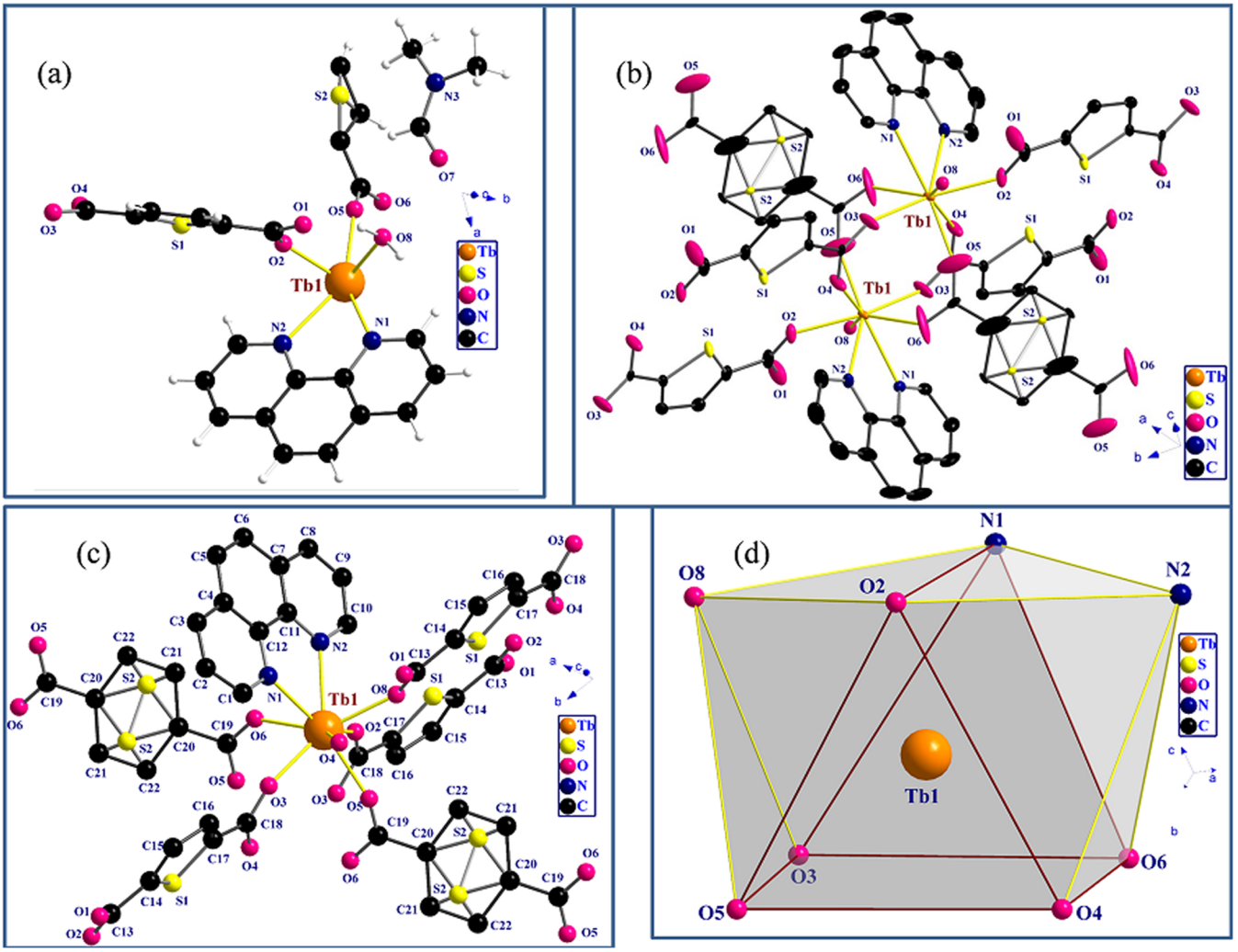

Figure 3. Pictographic representation of the crystal structure of Ln-CP **3**; (a) asymmetric unit; (b) ORTEP view of the structural unit (the thermal displacement ellipsoids are drawn at 50% probability; H atoms of guest DMF are omitted for structural clarity); (c) coordination environment of Tb1; and (d) square antiprismatic polyhedral geometry around the Tb1 center.

distances of 4.472 Å (Nd1···Nd1) and 4.231 Å (Nd2···Nd2). The two subunits constituting the SBU in CP **2** are linked together through two 2,5-TDC^{2-} moieties via the tridentate bonding mode (see Figure 2a). These tetranuclear [Nd_4] SBUs when extended linearly along the "*b*-axis" produce one-dimensional (1D) infinite rod-shaped polymeric chains (Figure 2b). These SBU chains are further linked together by a 2,5-TDC^{2-} spacer along the *ac*-plane, which leads to the formation of an infinitely growing 2D polymeric framework arranged in various packing arrangements (see Figure S1, Supporting Information).

For Ln-CP **2**, the Nd−O (COO^-) bond lengths are in the range from 2.3705 (15) to 2.5737 (18) Å and Nd−N bond lengths vary from 2.6169 (18) to 2.7138 (18) (see Table S3, Supporting Information) and the bond angles of O−Nd−O, N−Nd−N, and O−Nd−N are in the range of 65.03 (6)−143.18 (5)°, 60.46 (6)−62.45 (6)°, and 68.92 (5)−153.82 (6)°, respectively (see Table S4, Supporting Information), which are in agreement with the previously reported lanthanide(III) carboxylate-based coordination polymers.[113,114]

Figures S2−S4 represent the 2D polyhedral packing arrangements of CP **2** along three variable axes. There exists a widespread hydrogen bonding network between the various donor and acceptor pairs generated by the carboxylate groups and sulfur atom of 2,5-TDC^{2-}, N atoms of 1,10-Phen, and O and H atoms of the coordinated molecule, which assists in reinforcing the covalent interactions and to create a stable three-dimensional (3D) supramolecular architecture (Figure S5, Supporting Information). Topologically, the structure consists of 6-connected [3^2,5,6-c net] with the *sql* topology generated by joining Nd^{3+} centers (Figure 2c). The 2D space-filling model for CP **2** along the *c*-axis is shown in Figure 2d.

*Structural Description of {[Tb(2,5-TDC)$_{1.5}$(1,10-Phen)-(H$_2$O)]·DMF}$_n$ (**3**).* Single-crystal X-ray diffraction studies reveal that the synthesized CP having the formula {[Tb(2,5-TDC)$_{1.5}$(1,10-Phen)(H_2O)]·DMF}$_n$ crystallizes in the centrosymmetric $P\bar{1}$ space group of the triclinic crystal system, forming a 2D polymeric framework with a unit cell volume of 1251.90 (9) (for details, see Table 1). The crystallographically characterized independent part of CP **3** has one Tb^{3+} ion, one 1,10-Phen unit, one and half fully deprotonated 2,5-TDC^{2-}, one coordinated water molecule, and one guest dimethylformamide (DMF) molecule (Figure 3a). The two symmetrically distinct 2,5-TDC moieties and 1,10-Phen ligands exhibit three bonding modes. The 2,5-TDC moieties feature μ^4-κ^4,

https://doi.org/10.1021/acsomega.2c05179
ACS Omega 2022, 7, 41370−41391

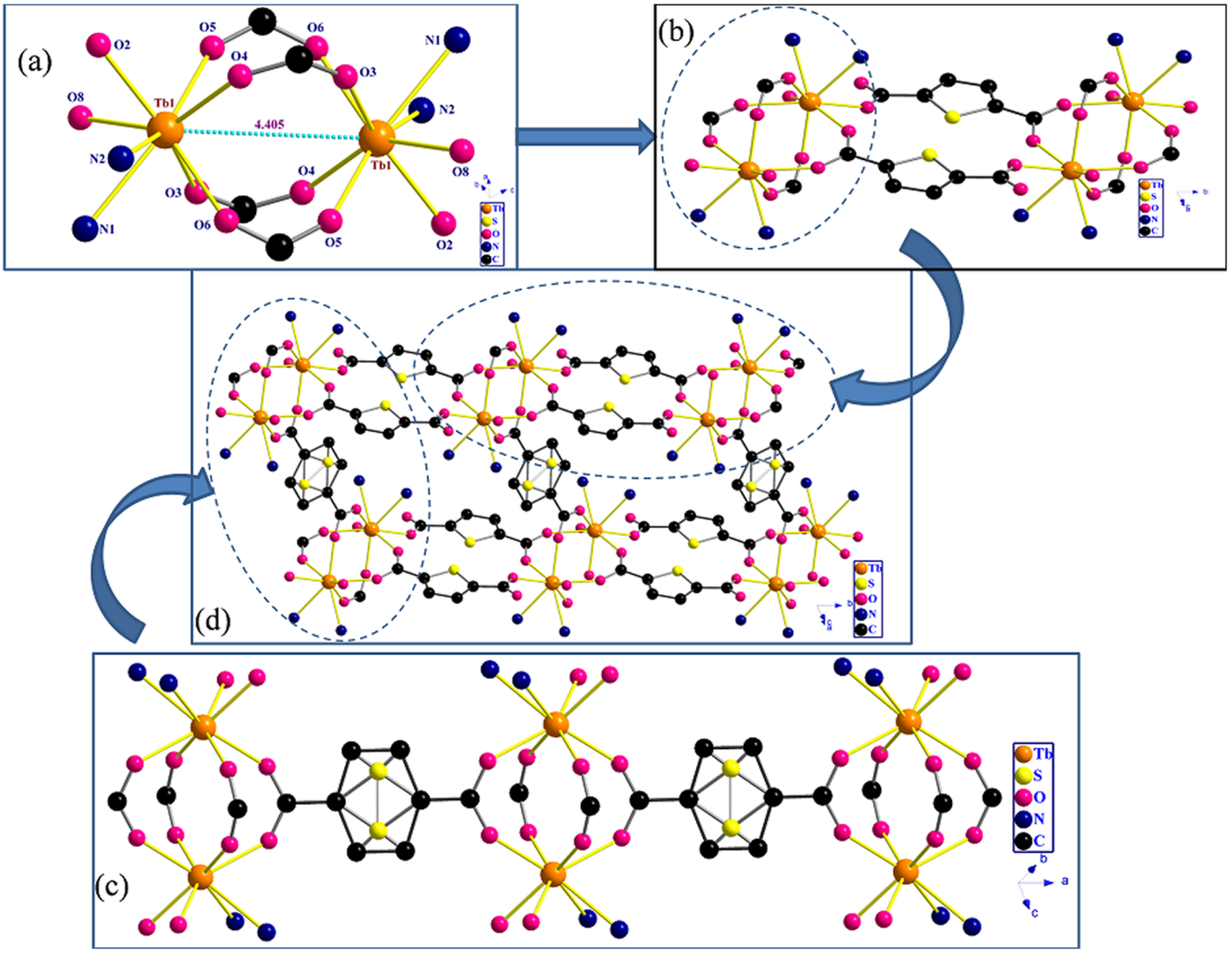

Figure 4. (a) Representation of the dinuclear $Tb_2O_{12}N_2$ SBU of Ln-CP **3**; (b) tetranuclear unit of SBU; (c) linear extension of SBU connected with the distorted 2,5-TDC moiety; and (d) 2D sheet-like extension of the tetranuclear SBU.

$\eta^1{:}\eta^1{:}\eta^1{:}\eta^1$ and μ^3-κ^3, and $\eta^1{:}\eta^1{:}\eta^1$ coordination modes, while 1,10-Phen exhibits the μ^1- κ^2, $\eta^1{:}\eta^1$coordination mode (see Scheme 1a,b,d).

The ORTEP view of CP 3 is depicted in Figure 3b. Thermal displacement ellipsoids are portrayed at 50% probability. The interstitial guest molecules and H atoms are eliminated for structural clarity in the ORTEP view. The surrounding environment as depicted in Figure 3c reveals that each Tb1 is coordinated to one 1,10-Phen, five fully deprotonated 2,5-TDC moieties, and one coordinated water molecule. Unexpectedly, out of the five 2,5-TDC moieties, two 2,5-TDC moieties show ring distortion, in which two thiophene rings get fused. Moreover, oxygen atoms O2, O3, O5, O6, and O8 originate from five unidentate carboxylates of five symmetrically nonequivalent 2,5-TDC ligands. Out of these five oxygen atoms, three oxygen atoms i.e., O2, O3, and O8, stem from three symmetry-equivalent 2,5-TDC units, while O5 and O6 originate from distorted 2,5-TDC units, and one oxygen atom, i.e., O4 originates from one coordinated water molecule. Two nitrogen atoms N1 and N2 stem from 1,10-phenanthroline through the bidentate chelating mode.

Two Tb(III) centers are bridged through O3, O4, O5, O6, O3#, O4#, O5#, and O6# via the bidentate bridging mode of the carboxylate group of four distinct 2,5-TDC units. The $[O_6N_2]$ donor set creates square antiprismatic polyhedral geometry around the Tb1 ion (Figure 3d). The Tb−O (COO^{2-}) and Tb−N bond lengths vary from 2.310 (3) to 2.423 (3) Å and 2.571 (3) to 2.594 (3) Å, respectively (see Table S5), and the bond angles of O−Tb−O are in the range of 71.66 (11)−146.14 (11) Å, while O−Tb−N bond angles are in the range of 70.42 (11)−148.51 (12) (see Table S6).[115,116] In the dimeric $Tb_2O_{12}N_4$ secondary building unit (SBU), the Tb1···Tb1 distance is 4.405 Å (Figure 4a). Two dinuclear SBUs are connected together through two 2,5-TDC ligands via the tridentate bonding (μ^3-κ^3, $\eta^1{:}\eta^1{:}\eta^1$) mode, forming a tetranuclear unit as shown in Figure 4b. These tetramer units of $[Tb_4]$ SBUs when extended linearly along the *bc*-plane generate 1D linear infinite rod-shaped chains (Figure 4c).

These extended 1D linear chains are further linked to each other through the distorted 2,5-TDC moiety via the tetradentate bonding mode to form a 2D sheet-like architectural framework (see Figure 4d). Figure S6 displays the packing arrangements of CP **3** when viewed along variable axes (*a*, *b*, and *c* axes). There exist noncovalent hydrogen bonding interactions generated by the carboxylate groups of $2,5\text{-}TDC^{2-}$, N atoms of 1,10-Phen, and O atoms of guest DMF and coordinated water molecule, which assist in reinforcing the

https://doi.org/10.1021/acsomega.2c05179
ACS Omega 2022, 7, 41370−41391

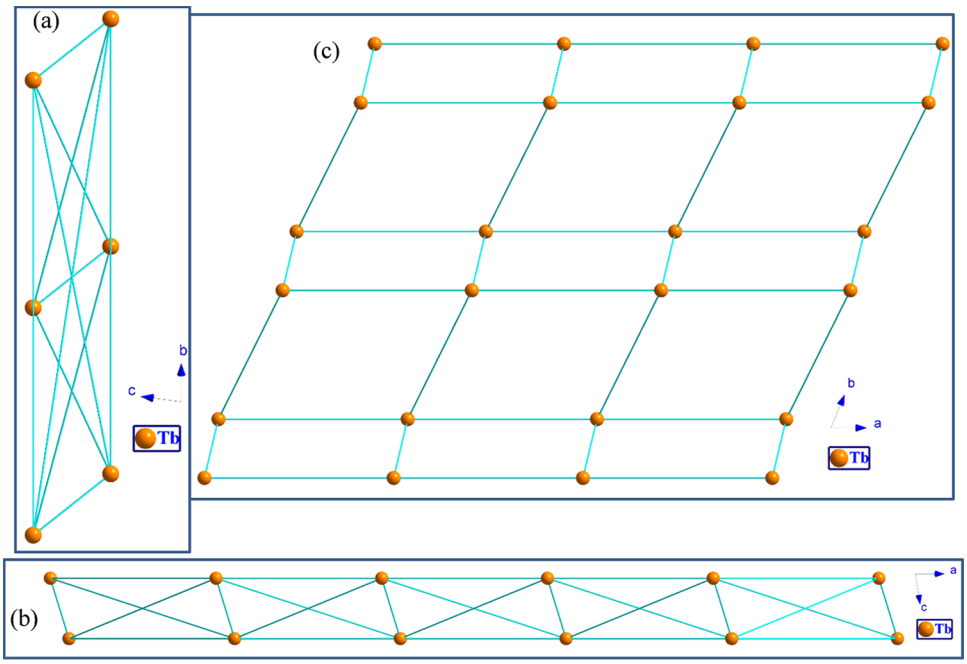

Figure 5. Topology of CP **3** along (a) *a*, (b) *b*, and (c) c axes.

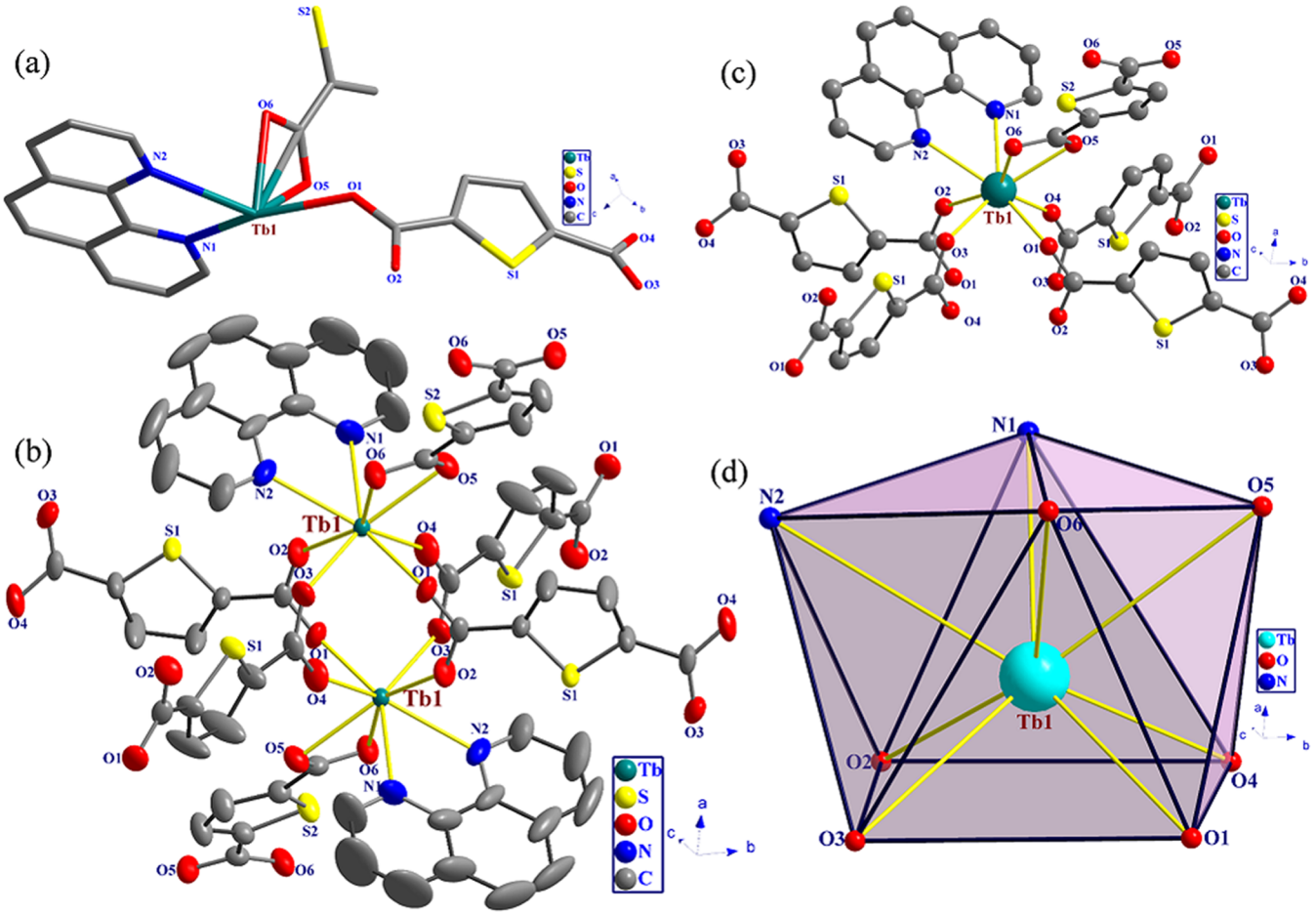

Figure 6. Pictographic representation of the crystal structure of CP **4**; (a) asymmetric unit of CP **4**; (b) ORTEP view of the structural unit (the thermal displacement ellipsoids are drawn at 50% probability; H atoms are omitted for structural clarity); (c) coordination environment of Tb1; and (d) square antiprismatic polyhedral geometry around the Tb1 center.

https://doi.org/10.1021/acsomega.2c05179
ACS Omega 2022, 7, 41370−41391

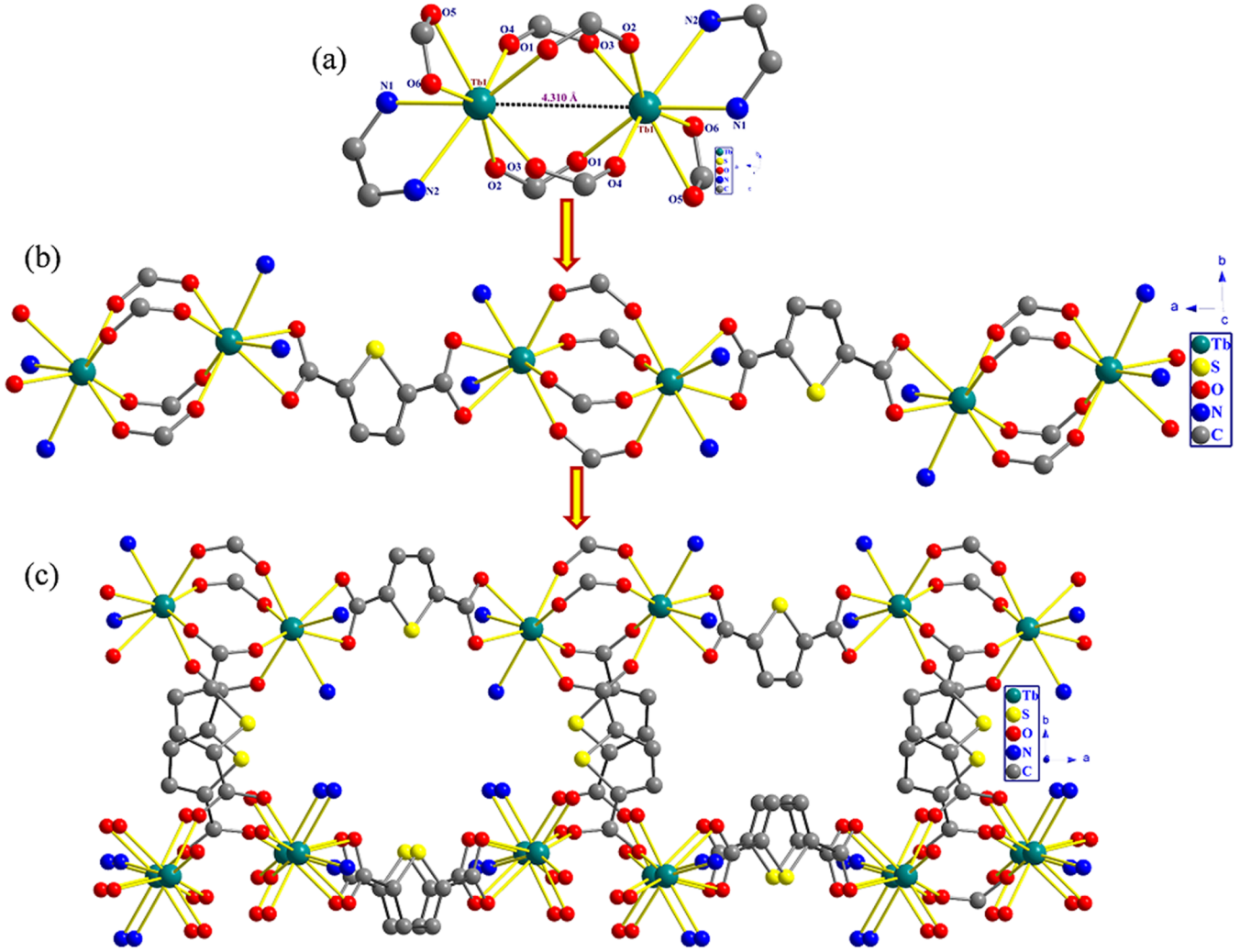

Figure 7. (a) Representation of the dinuclear $Tb_2O_{12}N_2$ SBU of CP **4**; (b) linear extension of the SBU connected with the 2,5-TDC moiety; and (c) 3D extension of the 1D linear chain.

covalent interactions and creating a stable three-dimensional (3D) supramolecular architecture (Figure S7, Supporting Information).

Moreover, interlayer $\pi\cdots\pi$ stacking interactions between 1,10-Phen rings and lp$-\pi$ interactions between the lone pair of the sulfur atom of 2,5-TDC and 1,10-Phen also improve the strength of the architectural framework. Figures S8−S10 represent the polyhedral packing arrangements of CP **3** along three variable axes. Topologically, the structure consists of 7-connected [3^6,7-c net] with *sql* topology generated by joining Tb^{3+} centers. The topological views of CP **3** along variable axes are depicted in Figure 5a−c.

*Structural Description of [Tb(2,5-TDC)$_{1.5}$(1,10-Phen)] (**4**).* X-ray crystallographic studies depict that the synthesized CPs **4**−**8** are isomorphous and crystallize in the monoclinic *C*2/*c* space group, forming a 3D polymeric structure with the unit cell volume ranging from 4684.02 (18) to 4830.34 (6) Å; for details, see Table 1. Moreover, in the case of CP **5** and **6**, two water molecules are present in the lattice, as we have used the mask command to solve the structure. All the five CPs **4**−**8** are isostructural and show similar coordination features. Therefore, herein, we discuss the detailed structural features of CP **4** (Tb) as a representative example.

The crystallographically characterized asymmetric unit of CP **4** has one Tb(III) ion, one and a half fully deprotonated 2,5-TDC^{2-} unit, and one 1,10-Phen (Figure 6a). The rigid 2,5-TDC^{2-} linker features two different bonding modes, viz., μ_2-κ^4, η^1:η^1:η^1:η^1 and μ_4-κ^4, η^2:η^2, whereas 1,10-Phen exhibits the μ_2-κ^4,η^1:η^1 coordination/bonding mode (see Scheme 1a,c,d).

The ORTEP view of CP **4** is depicted in Figure 6b (wherein H atoms are partially omitted for structural clarity). The surrounding environment of the Tb(III) ion is portrayed in Figure 6c, which indicates that the Tb(III) ion is eight-coordinated and surrounded by the [O_6N_2] donor set. The [O_6N_2] donor set consists of six oxygen atoms (viz., O1, O2, O3, O4, O5, and O6) of carboxylate units stemming from five different 2,5-TDC^{2-} linkers and two nitrogen atoms (N1 and N2) from the coordinated 1,10-Phen ligand, thereby forming square antiprismatic geometry with D_{4d} symmetry as shown in Figure 6d.

The oxygen atoms O1, O2, O3, and O4 derived from the symmetry-equivalent four carboxylates of four distinct 2,5-TDC^{2-} ligands are bonded via the unidentate bonding mode, while O5 and O6 stemming from the same carboxylate of one 2,5-TDC^{2-} are linked by the bidentate chelating mode. Nitrogen atoms N1 and N2 stemming from the phenanthroline ring are bonded in the bidentate chelating mode (as shown

https://doi.org/10.1021/acsomega.2c05179
ACS Omega 2022, 7, 41370−41391

Table 2. Structural Features of Ln-CPs 1−8

CPs	crystal system	empirical formula	Ln(III) centers	Ln···Ln	C. no.	geometry
1 (Pr)	triclinic ($P\bar{1}$)	$[Pr_2(2,5\text{-TDA})_3(1,10\text{-Phen})_2(H_2O)_2]_n$	Pr1	4.500	8	square antiprismatic
			Pr2	4.202	8	bicapped trigonal prismatic
2 (Nd)	triclinic ($P\bar{1}$)	$[Nd_2(2,5\text{-TDA})_3(1,10\text{-Phen})_2(H_2O)_2]_n$	Nd1	4.472	8	square antiprismatic
			Nd2	4.231	8	bicapped trigonal prismatic
3 (Tb)	triclinic ($P\bar{1}$)	$\{[Tb(2,5\text{-TDA})_{1.5}(1,10\text{-Phen})(H_2O)]\cdot DMF\}_n$	Tb1	4.405	8	square antiprismatic
4 (Tb)	monoclinic ($C2/c$)	$[Tb(2,5\text{-TDA})_{1.5}(1,10\text{-Phen})]_n$	Tb1	4.310	8	square antiprismatic
5 (Dy)	monoclinic ($C2/c$)	$[Dy(2,5\text{-TDA})_{1.5}(1,10\text{-Phen})]_n$	Dy1	4.304	8	square antiprismatic
6 (Ho)	monoclinic ($C2/c$)	$[Ho(2,5\text{-TDA})_{1.5}(1,10\text{-Phen})]_n$	Ho1	4.295	8	square antiprismatic
7 (Er)	monoclinic ($C2/c$)	$\{[Er(2,5\text{-TDA})_{1.5}(1,10\text{-Phen})]\cdot H_2O\}_n$	Er1	4.280	8	square antiprismatic
8 (Yb)	monoclinic ($C2/c$)	$[Yb(2,5\text{-TDA})_{1.5}(1,10\text{-Phen})]_n$	Yb1	4.267	8	square antiprismatic

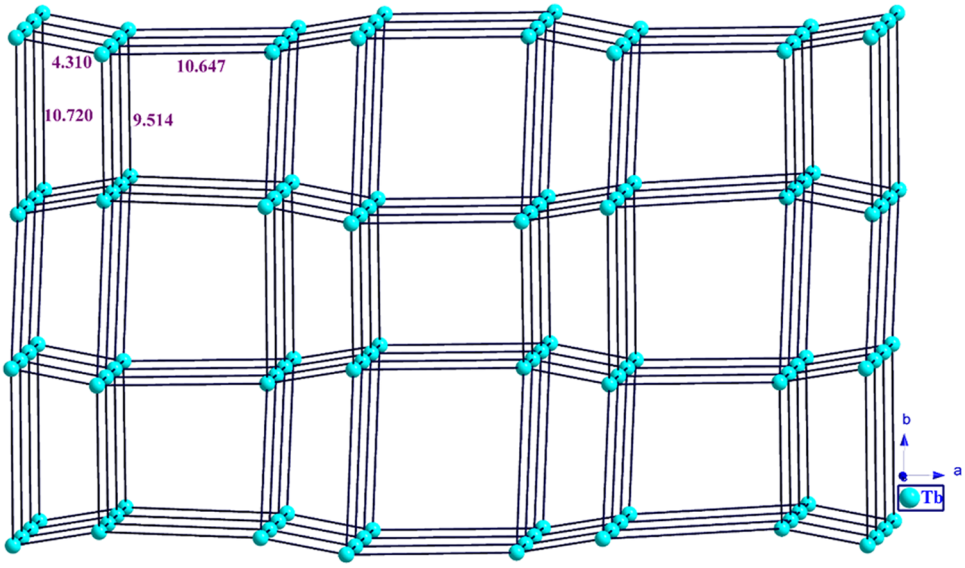

Figure 8. Topology of CP **4**.

in Scheme 1d). The O1, O1#, O2, O2#, O3, O3#, O4, and O4# atoms of 2,5-TDC^{2-} units form a tetradentate chelating bridge between Tb1 and Tb1, forming a dimeric $[Tb_2O_{12}N_4]$ secondary building unit (SBU), as shown in Figure 7a. These SBUs are linked through O5 and O6 atoms of each 2,5-TDC^{2-} moiety via the tetradentate chelating mode, forming an infinite 1D linear chain along the *c*-axis (Figure 7b). These 1D chains are further linked together along the *ab*-plane through 2,5-TDC in the tetradentate bonding mode, leading to the formation of a 3D polymeric architectural framework (Figure 7c). The packing arrangements of CP **4** when viewed along variable axes (*a*, *b*, and *c* axes) are displayed in Figure S11. The Tb1···Tb1 SBU separation in the binuclear motif is 4.310 Å. The Tb−O and Tb−N bond lengths are in the range of 2.3065 (18)−2.4903 (18) and 2.532 (3)−2.593 (2) Å, respectively (see Table S7), which are typical for the lanthanide carboxylate (Ln−OOC) coordination bonds, whereas the O−Tb−O, O−Tb−N, and N−Tb−N bond angles are in the range from 53.24 (6) to 146.46 (7), 70.90 (7), −145.59 (8), and 63.87 (10), respectively (see Table S8).[115,116] The polyhedral packing array of CP **4** along the *a*, *b*, and *c* axes is projected in Figures S12−S14, Supporting Information.

In CPs **1**−**8**, the Ln−O bond lengths decrease with increasing atomic number and lie in the range of 2.897−2.436 Å. In dimeric $Ln_2O_{12}N_4$ secondary building units (SBUs), the inter-lanthanide(III) distances (Ln···Ln) exhibit a regular decrease with the increase in the atomic number from 4.5 Å in CP **1** (Pr) to 4.267 Å in CP **8** (Yb). The Ln···Ln separation trends are consistent throughout all the CPs. Important structural parameters of the Ln^{3+} ions in CPs **1**−**8** are tabulated in Table 2. The hydrogen bonding interactions between various acceptor and donor pairs such as carboxylates groups and the sulfur atom of 2,5-TDC^{2-} and N atoms of 1,10-Phen assist in reinforcing the covalent interactions within the structural motifs and thus produce a robust 3D supramolecular framework (see Figure S15, Supporting Information). Moreover, the SBUs of all the CPs are depicted in Figures S16−S20, Supporting Information. In addition, interlayer $\pi\cdots\pi$ stacking interactions between 1,10-Phen rings and lp−π interactions between the sulfur atoms of 2,5-TDC^{2-} and 1,10-Phen improve the strength of the architectural framework.

To better interpret the 3D framework of CP **4**, a topological analysis was done using TOPOS Pro. Topologically, each eight-coordinated Ln(III) ion acts as a 7-connected network linked by the 2,5-TDC^{2-} anion (μ_2-κ^4, η^1:η^1:η^1:η^1) and (μ_4-κ^4, η^2:η^2) as rigid linkers. The existence of tetradentate (μ_2-κ^4, η^1:η^1:η^1:η^1) and bidentate chelating (μ_4-κ^4, η^2:η^2) modes of the 2,5-TDC^{2-} anion results in the formation of alternate rectangular and trapezium arrays of Ln^{III} ions. The 3D connected topological network consisting of [3^3,7-c net] with the *xah* topological net of Ln-CP **4** is depicted in Figure 8.

Conclusively, we present a comparative discussion on the structural features (mainly coordination features and packing arrangements) of CPs **1**−**8**, and we classified them into two

https://doi.org/10.1021/acsomega.2c05179
ACS Omega 2022, 7, 41370−41391

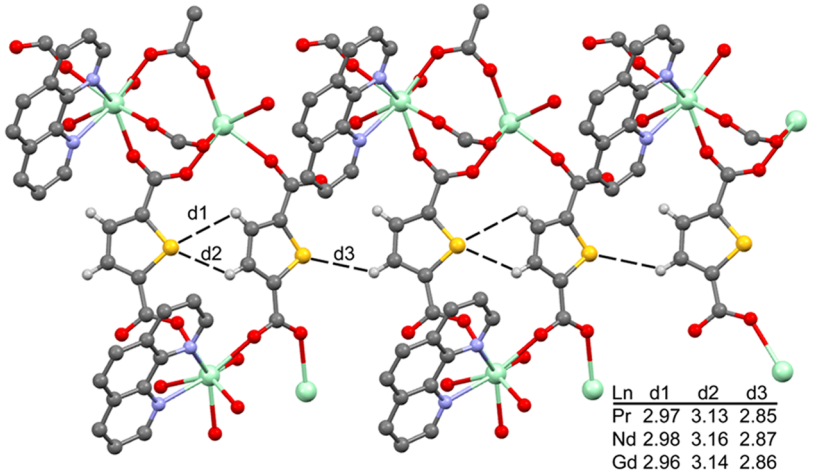

Figure 9. Partial view of the X-ray structure representing the CPs of Pr and Nd. Distances in Å.

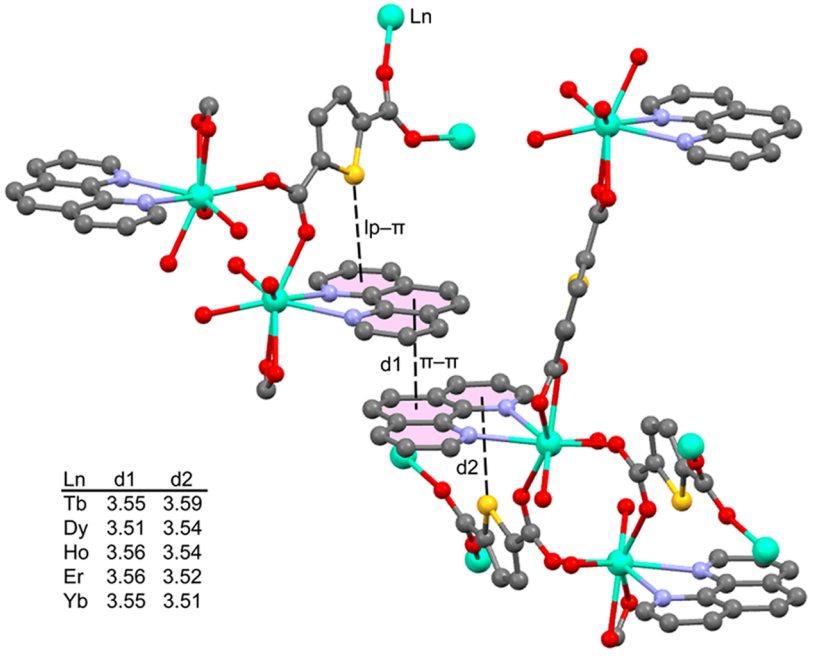

Figure 10. Partial view of the X-ray structure representing the CPs of Tb, Dy, Ho, Er, and Yb. Distances in Å measured to the ring centroid for the lp−π and between the ring centroids of the central aromatic rings for the π−π interaction.

groups: "group A" constitutes 2D CPs **1**−**3** and "group B" constitutes 3D CPs **4**−**8**. Furthermore, "group A" constitutes two subgroups: one consists of CPs **1** and **2** and the other subgroup consists of only CP **3**. Now, we have chosen CP **2** (Nd) from the first subgroup to compare with CP **3** and CP **4** from "group B." Compound **2** (Nd) generates a tetranuclear $[Nd_4O_{24}N_4]$ SBU with Ln···Ln distances of 4.472 Å, (Nd1···Nd1) and 4.231 Å (Nd2···Nd2), while both CP **3** and CP **4** generate dinuclear $[Tb_2O_{12}N_4]$ SBUs with Tb1···Tb1 distances of 4.405 and 4.310 Å, respectively. In CPs **2** and **3**, the 2,5-TDC^{2-} moiety shows tetradentate μ_4-κ^4, η^1:η^1:η^1:η^1 and tridentate μ_3-κ^3,η^1:η^1:η^1:η^0 bonding modes (Scheme 1a,b), while in CP **4**, it displays tetradentate μ_4-κ^4, η^1:η^1:η^1:η^1 and tetradentate chelating μ_4-κ^4, η^2:η^2 modes (Scheme 1a,c). Additionally, in the coordination environment of CP **3**, out of five 2,5-TDC moieties, thiophene rings of two 2,5-TDC moieties show ring distortion (Figure 3c). In CP **2**, the two crystallographically distinct Ln^{3+} centers (Nd1 and Nd2) feature eight coordination number corresponding to the square antiprismatic and bicapped trigonal prismatic geometries, respectively (see Figure 1c,d), whereas for both CP **3** and **4**, only one Ln^{3+} center (Tb1 and Tb1) exhibits eight coordination number having a square antiprismatic geometry (see Figures 3d and 6d). As mentioned above, threecompounds of **1**−**3** belonging to the triclinic $P\bar{1}$ crystal structures constitute two isomorphous subgroups. The second isomorphous subgroup (CP **3**) can be differentiated from the first subgroup (CP **1**−**2**) in the packing arrangements when viewed along variable axes as depicted in Figures S1 and S6. All these structural evolutions between three types of CPs arise due to the (i) change in the solvent system as mentioned in the synthesis section and (ii) the difference in the bonding mode of the linker 2,5 TDC also seems to play an important role due to the difference in the bidentate and tetradentate chelating modes of the same, giving rise to 2D and 3D CPs, respectively.

https://doi.org/10.1021/acsomega.2c05179
ACS Omega 2022, 7, 41370−41391

Density Functional Theory (DFT) Calculations. The theoretical study is focused on the analysis of the π-stacking interaction adopted by the phenanthroline ligand in several CPs that is combined with lone pair (lp)$-\pi$ interactions involving the S atom of the 2,5-thiophenedicarboxylic acid, forming interesting lp$-\pi/\pi-\pi/$lp$-\pi$ assemblies. In fact, the examination of the solid-state structures of the CPs reported herein suggests that the lp$-\pi$ interaction is competitive with H bonds (HBs), that is, for the CPs with Ln = Pr and Nd; the thiophene rings form infinite 1D chains propagated by H-bonding interactions (see Figure 9) with S···H distances ranging from 2.85 to 3.16 Å. In contrast, such H-bonded assemblies are not formed in the rest of CPs, where the S atom of the thiophene ring points to the center of one of the fused aromatic rings of the coordinated 1,10-phenanthroline ligand, thus forming the lp$-\pi/\pi-\pi/$lp$-\pi$ assemblies represented in Figure 10. Both the lp$-\pi$ and $\pi-\pi$ interactions exhibit similar distances, 3.51−3.59 Å.

Since the compounds reported herein are polymeric, we have used theoretical models as minimalistic models of the experimental structures. A generic model is represented in Figure 11, where each lanthanide is coordinated to phenanthroline, 2,5-thiophenedicarboxylate, two formate anions, and two formic acids to preserve the neutrality and the coordination number of the metal centers. The MEP surface for Ln = Tb is represented in Figure 11b, showing that the most positive and negative MEP values are located in parts of the complex that have been theoretically modified compared to the real system. Therefore, we have indicated in the figure those values in the regions that better represent the CPs. It can be observed that the MEP at the coordinated O atom of the carboxylate group is large and negative (−36.4 kcal/mol). Moreover, the MEP at the S atom is also negative (−18.8 kcal/mol), thus adequate for interacting with electrophilic regions. Interestingly, the MEP values over the phenanthroline rings are positive (around 10 kcal/mol), thus revealing that its coordination to the metal center makes the aromatic ring electron-deficient and thus adequate to establish interactions with electron-rich atoms. This explains the formation of the lp$-\pi$ interactions represented in Figure 10.

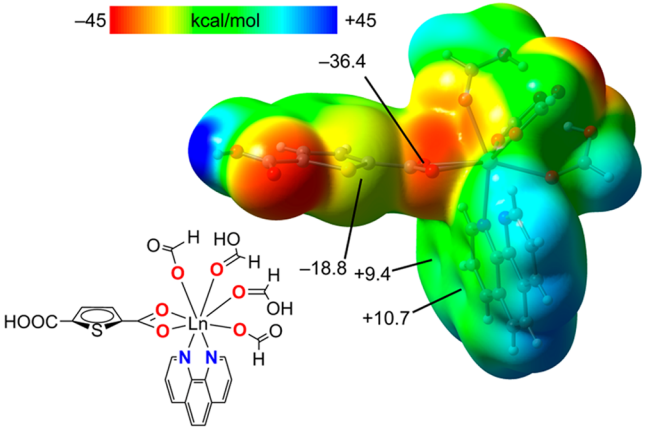

Figure 11. (a) Generic theoretical model used in this work. (b) MEP surface of the model for Ln (Tb = Nd) at the PBE0-D3/def2-TZVP level of theory. (The energies at selected points of the surface are given in kcal/mol).

As mentioned above, energetic DFT analysis is devoted to analyzing the lp$-\pi$ and $\pi-\pi$ stacking interactions that have a relevant structure-directing role in the solid state of most of the CPs reported herein. To roughly estimate the lp$-\pi$ interaction, we have compared two rotamers, as shown in Figure 12. The rotamer shown in Figure 12a corresponds to the conformation observed in the solid state and that shown in Figure 12b corresponds to the theoretical model where the thiophene ring has rotated 180° in such a way that the S···π is not established. The experimentally observed rotamer is 3.2 kcal/mol lower in energy, thus suggesting that the strength of the lp$-\pi$ interaction is at least −3.2 kcal/mol, since in the theoretical rotamer, a very weak CH···π is likely contributing to its stabilization.

Figure 13a shows the lp$-\pi/\pi-\pi/$lp$-\pi$ assembly using Ln = Nd as a representative CP. The interaction energy is large and negative (ΔE = −17.7 kcal/mol), thus suggesting that this assembly is indeed relevantly influencing the solid-state architecture of CPs **1**−**3**. Figure 13b shows the combined QTAIM/NCIPlot analysis of the whole assembly. The combination of QTAIM and NCIPlot in the same representation is very convenient to characterize noncovalent interactions in real space. It can be observed that the lp$-\pi$ is characterized by one bond critical point (BCP, red sphere) and bond path (dashed lines) connecting the S atom of the thiophene ring to one C atom of the coordinated 1,10-

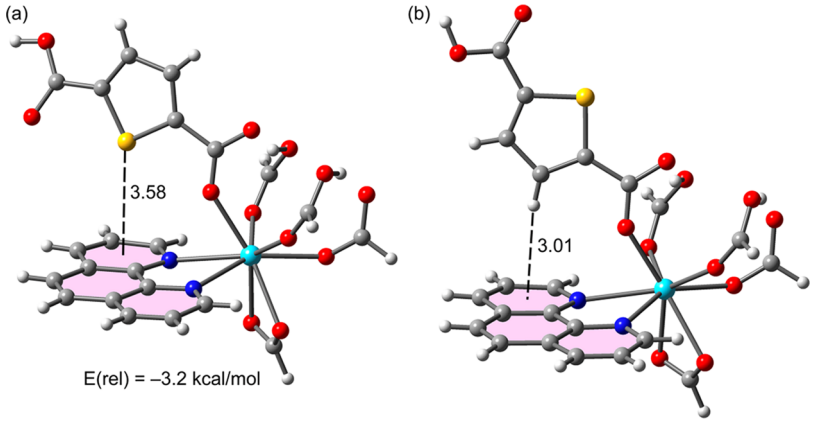

Figure 12. Two rotamers of a generic model of CPs **1**−**3** (a) corresponding to the X-ray structure and (b) theoretical one where the thiophene ring has been rotated to 180° (distances in Å).

https://doi.org/10.1021/acsomega.2c05179
ACS Omega 2022, 7, 41370−41391

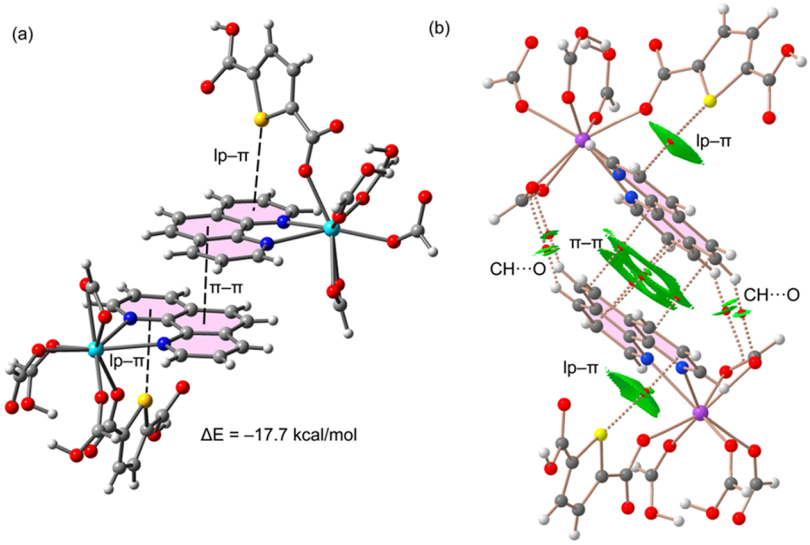

Figure 13. (a) Theoretical model used to evaluate the π-stacking interaction. (b) QTAIM/NCIPlot analyses of intermolecular bond CPs (red spheres) and bond paths of the lp$-\pi/\pi-\pi/$lp$-\pi$ assembly. Only intermolecular interactions are represented. The dimerization energies at the PBE0-D3/def2-TZVP level of theory are also indicated.

phenanthroline ligand, thus confirming the interaction. Moreover, an extended green NCIPlot isosurface embraces the region between the S atom and one of the six-membered rings of the ligand coincident to the location of the bond CP. This distribution of BCPs, bond paths, and reduced density gradient (RDG) isosurfaces support the lp$-\pi$ nature of this interaction. The $\pi-\pi$ stacking is characterized by four BCPs and bond paths interconnecting several C atoms of both aromatic rings. The extended NCIPlot RDG isosurface embraces two six-membered rings of the ligands (the aromatic ring that forms the lp$-\pi$ interaction does not participate in the π-stacking).

The QTAIM/NCIPlot analysis also reveals the formation of two ancillary CH···O HBs involving aromatic CH bonds and formate ligands, also characterized by a BCP and bond path. We have calculated the contribution of these HBs using the methodology proposed by Espinosa et al.[117] that estimates the dissociation energy using the potential energy density (Vr) at the BCP ($E_{dis} = -1/2 \times Vr$). As a result, the computed CH···O interaction is very weak (−0.4 kcal/mol each one), thus evidencing the dominant nature of the π-stacking interaction.

FTIR Spectroscopy. The vibrational bands show a similar pattern for the synthesized CPs **1**−**8** as depicted in Figures S21−S24, Supporting Information. Broad and strong bands appearing in the 3502−3487 cm^{-1} region are assigned to the stretching vibrations of coordinated/surface-absorbed water molecules.[41] The two bands appearing in the range of 1641−1633 and 1526−1518 cm^{-1} are due to the asymmetric stretching modes, and one band appearing in the region of 1386−1369 cm^{-1} corresponds to the symmetric stretching modes of carboxylic groups. The absence of the characteristic asymmetric vibrations in the range of 1780−1680 cm^{-1} of carboxylate groups confirms the full deprotonation of 2,5-thiophenedicarboxylic acid residues on coordination to Ln^{3+} centers as revealed from single-crystal X-ray analysis.[118] The characteristic band appearing in the regions of 2973−2918 and 1252−1022 cm^{-1} are attributed to the υ_{C-H} stretching vibrations and −CH− out-of-plane bending modes of the 2,5-TDA^{2-} linker, respectively. Distinct IR bands in the 900−400 cm^{-1} region are allocated to Ln(III) carboxylate vibrations.[119]

Powder X-ray Diffraction. To investigate the isostructurality and to check the phase purity of the obtained polycrystalline samples of CPs **1**−**8**, powder X-ray diffraction data are recorded. The simulated pattern acquired from single-crystal XRD is in good agreement with the experimental pattern as depicted in Figures S25−S27, Supporting Information. The minor difference in the relative intensities of PXRD patterns may be due to the preferred orientation of powder crystal samples applied for recording the PXRD data.[119]

Thermogravimetric Analysis. Thermal stability of coordination polymers is a crucial parameter for their probable applications as functional materials. The thermal decomposition behavior of CPs **2** (Nd) (triclinic; $P\bar{1}$), **3** (Tb) (triclinic; $P\bar{1}$), and **8** (Yb) (monoclinic;$C2/c$) as representative members of three different structural types have been explored in detail (as shown in Figure S28, Supporting Information). Thermal analysis of the assembled CPs was performed under an inert N_2 atmosphere in the temperature range of 30−950 °C at a heating rate of 10 °C/min. Compounds **2** (Nd) and **3** (Tb) feature typical three-step and compound **8** (Yb) exhibits two-indistinguishable step weight loss behavior (pink, blue, and gray curves in Figure S28, Supporting Information, for CPs **2**, **3**, and **8**, respectively). It is clearly apparent that compound **2** is thermally stable up to 130 °C. The first step of weight loss is due to the removal of the coordinated water molecule (onset of 150 °C). In the second step, decoordination of 1,10-phenanthroline molecules takes place, (onset of 390 °C) followed by the rapid decomposition and collapse of the whole structural framework in the third step. Compound **3** is thermally stable up to 70 °C. The first step of weight loss is due to the removal of the uncoordinated DMF molecule (onset of 76 °C). In the second step, removal of the coordinated water molecule (onset of 330 °C) takes place, followed by the rapid decomposition and collapse (onset of 390 °C) of the whole structural framework in the third step. It is apparent that CP **8** is thermally stable up to 340 °C, depicting significant thermal stability. The first step of weight loss is attributed to the loss of coordinated 1,10-phenanthroline molecules (onset of 350 °C), followed by rapid collapse

https://doi.org/10.1021/acsomega.2c05179
ACS Omega 2022, 7, 41370−41391

and decomposition of the structural framework of CP in the second step (onset of 460 °C). Indeed, in comparison to CP **2** (Nd) and CP **3** (Tb), CP **8** has appreciable thermal stability, as it starts decomposing at a higher temperature (350 °C). This difference can be attributed to the absence of water molecule(s) in the coordination sphere of CP **8**.

Photoluminescence Properties of Ln-CP 4. Lanthanide ions possess unique optical characteristics attributed to the 4f–4f electronic transitions. The interaction between the 4f orbitals and the surrounding environment is quite weak due to the shielding effect exerted on the 4f orbitals. This reduces the oscillator strength in the f–f transitions.[119] Therefore, an appropriate choice of Ln ions (Tb^{3+}, Eu^{3+} etc.) and organic linker becomes crucial in designing the desired Ln-CPs exhibiting excellent luminescence properties.[120] Terbium ions as the metal component of Ln-CPs have acquired special attention for optical studies, as they display excellent luminescence properties due to their longer excited lifetimes, sharp strong emissions, and high color purity, which can generate strong luminescence signals with visible emission colors and high quantum efficiencies.[121] As Tb(III) ions display Laporte-forbidden 4f → 4f transitions, which have weaker molar absorption, it is difficult to excite them. To deal with this problem, π-conjugated systems (ligands) are mostly applied to prepare efficient luminescent lanthanide-based coordination frameworks with high molar absorption.[122] Here, 2,5-thiophenedicarboxylic acid and 1,10-phenanthroline are utilized, which act as highly absorbing struts harvesting energy and then transferring it to the coordinated Tb metal centers through the "antenna effect" in CPs. This increases the emission via metal-facilitated intersystem crossing energy transfer sensitization from singlet to triplet excited states of the linker and then to the metal, resulting in efficient luminescence from the Tb^{3+} ion. Therefore, the photophysical properties of CP **4** were explored at ambient temperature. Herein, the two synthesized Tb-based coordination polymers CPs **3** and **4** were employed for their luminescence properties. As shown in Figure S29, CP **4** exhibited excellent luminescence emission intensity in comparison to that of CP **3**. This was due to the presence of the solvent (DMF) in CP **3**, which enhanced nonradiative decay and hence decreases luminescence emission intensity.[123] Thus, CP **4** due to the excellent fluorescence behavior was further utilized in the sensing titration experiments toward different toxic nitroaromatic compounds at ambient temperature.

Upon excitation at 252 nm, CP **4** reveals the representative green luminescence of Tb^{3+} ions, as shown in the CIE plot with CIE coordinates (0.34, 0.58; Figure 14, inset). The emission peaks of Tb^{3+} ions at 493, 547, 589, and 620 nm correspond to the characteristic sharp and narrow transitions $^5D_4 \rightarrow {}^7F_6$, $^5D_4 \rightarrow {}^7F_5$, $^5D_4 \rightarrow {}^7F_4$, and $^5D_4 \rightarrow {}^7F_3$, respectively. Among them, the $^5D_4 \rightarrow {}^7F_5$ transition at 547 nm, as the strongest emission and highly sensitive magnetic dipole transition, is usually used in spectroscopic studies. No ligand-based emissions are observed, indicating the efficient/successful sensitization from the linker to the Tb^{3+} ion.

Chemical Sensing of CP 4: Screening of Nitroaromatic Compounds. The intense photoluminescence and excellent luminescence stability of CP **4** intrigue us to further explore it as a chemical sensor for nitroaromatic compounds. The luminescence spectrum of the aqueous solution of CP **4** is almost similar to the solid-state spectra upon excitation at 252 nm. Fluorescence measurements of CP

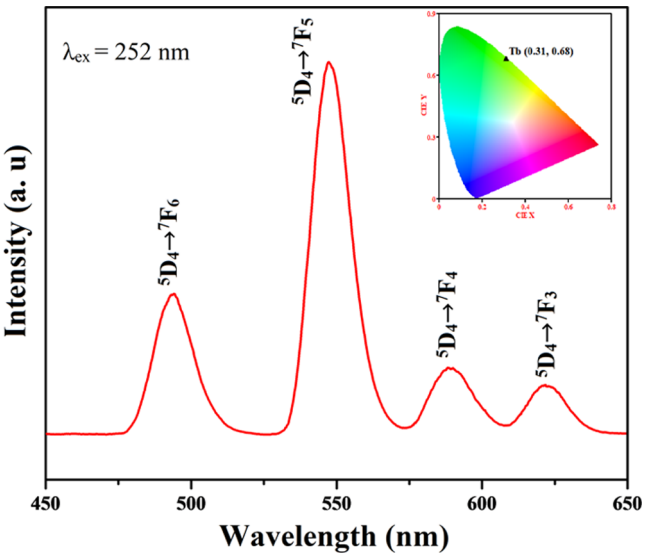

Figure 14. Emission spectrum of CP **4** recorded at room temperature (CIE plot inset).

4 are carried out at room temperature after ultrasonication treatment for 30 min for 1 h to ensure the homogeneity of the solutions. Aqueous solutions of various nitroaromatic analytes, namely, PA, *m*-DNB, *p*-NA, *m*-NA, *p*-NT, *p*-NP, and *o*-NBzA, ranging from 10 to 100 ppm are prepared, and luminescence quenching titrations are performed by adding increasing concentration of the solutions of nitroanalytes to the suspension of CP **4**.

The change in the intensity of emission peaks was monitored at 547 nm, attributed to the $^5D_4 \rightarrow {}^7F_5$ transition, as it is affected more regularly with addition of the analyte in comparison with other peaks. It is clearly illustrated in Figures 15 and S30–S35 that the emission intensity of CP **4** decreases concurrently with an increase in concentrations from 10 to 100 ppm for all nitroanalytes studied. However, the emission intensity of CP **4** in the presence of *p*-NT was almost completely quenched at 100 ppm concentration of the *p*-NT analyte. Remarkably, the fluorescence titration figure of *p*-NT clearly indicates the rapid attenuation of the fluorescence intensity of CP **4** from 29% at 10 ppm to 97% at 100 ppm *p*-NT (Figure 15a).

However, the addition of other nitroanalytes such as PA, *m*-DNB, *p*-NA, *m*-NA, *p*-NT, *p*-NP, and *o*-NBzA in an equivalent amount also exhibits quenching of emission bands of CP **4** but to a lesser extent when compared with that of *p*-NT under similar conditions (see Figures 15a and S30a–S35a). The quenching efficiency is calculated by $(I_0 - I)/I_0 \times 100$ (where I_0 and I are the luminescence intensities of CP **4** in the absence and presence of nitroanalytes, respectively). The quenching efficiencies for nitroanalytes fall in the order *p*-NT > *m*-NA > *m*-DNB > PA > *o*-NBzA > *p*-NP > *p*-NA. The most effective quencher is *p*-nitrotoluene (*p*-NT) and the least effective one is *p*-nitroaniline (*p*-NA), which do not corroborate well with their π-acidity trend. Importantly, the luminescence intensity of CP **4** is quenched completely (almost) when the concentration of *p*-NT is as low as 4.3×10^4 M^{-1}, indicating that compound **4** has a very low detection limit (LOD) value for *p*-NT.

For better understanding of the observed results of the quenching phenomenon and selectivity toward *p*-NT, the

https://doi.org/10.1021/acsomega.2c05179
ACS Omega 2022, 7, 41370–41391

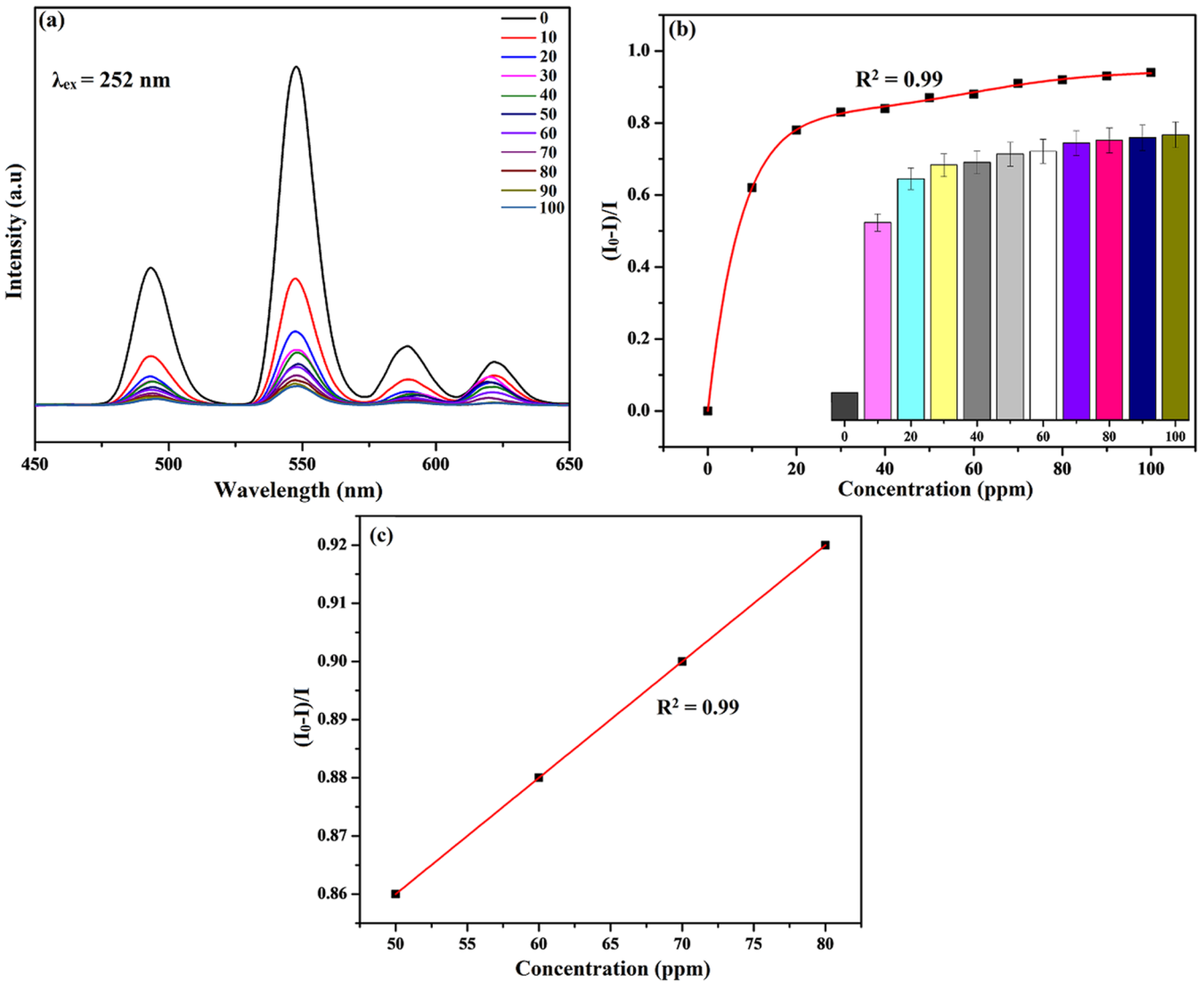

Figure 15. (a) Sensing properties of CP **4** in different aqueous concentrations of *p*-NT; (b) nonlinear Stern−Volmer plot of I_0-I/I versus [*p*-NT] concentration and error bar graph; and (c) linear Stern−Volmer fitting.

quenching coefficient/Stern−Volmer constant (K_{sv}) of CP **4** was evaluated using the Stern−Volmer equation $\{I_0/I = 1 + K_{sv}[M]\}$, (where I_0 is the initial luminescence intensity of CP **4** in the absence of nitroanalytes and I is the luminescence intensity of CP **4** in the presence of the nitroanalyte compound and [M] is the concentration of the nitroaromatic analyte) (as shown in Figures 15b and S30b−S35b). The calculated K_{sv} values for *p*-NT, *m*-NA, *m*-DNB, PA, *o*-NBzA, *p*-NP, and *p*-NA are 2.3×10^4, 1.6×10^4, 1.35×10^4, 1.0×10^4, 0.98×10^4, 0.85×10^4, and 0.82×10^4 M^{-1}, respectively. The decrease in fluorescence emission intensities of CP **4** confirms that the photoluminescence intensity is governed by the nitroanalyte concentration. The Stern−Volmer constants and quenching efficiency values for nitroaromatic compounds are enlisted in Table S17.

The extent of quenching (also denoted by K_{sv}) can be simply determined by plotting $(I_0/I - 1)$ versus molar concentrations of the added analytes. It consequently deviates from linearity, which may be due to the coexistence of static and dynamic quenching processes, self-absorption, and/or resonance energy transfer process between *p*-NT and CP **4** as shown in Figures 15b and S30b−S35b. However, it was observed that *p*-NT shows higher quenching efficiency even at a very lower concentration (10 ppm) in comparison to that of other taken analytes. The deviation in the S−V plot from linearity at lower concentrations also validates the superior quenching ability of *p*-NT over others.[124] Remarkably, the observed K_{sv} value for CP **4** with *p*-NT is 4.3×10^4 M^{-1} with a quenching efficiency of 97% at 100 ppm in aqueous solution, higher than that of the other nitroaromatic-based sensors. The quenching efficiencies for all other considered nitroanalytes are also calculated and displayed in Figure S36. To the best of our knowledge, this is the highest value of reported quenching constant for *p*-NT among all nearby lanthanide-based coordination polymers in aqueous media.

The limit of detection (LOD) was calculated for all the systems using the formula $3\sigma/S$, where 3 indicates the 95% confidence level factor; σ is the standard deviation of the observed intensity for blank CP **4** (without addition of nitroanalytes), and *S* is the slope of the linear calibration curve. The LOD values of all nitroaromatic analytes were calculated: *p*-NT (0.88 ppm), *m*-NA (1.1 ppm), *m*-DNB (1.4 ppm), PA (2.5 ppm), *o*-NBzA (2.9 ppm), *p*-NP (4.4 ppm), and *p*-NA (10 ppm). Remarkably, *p*-NT showed a minimum limit of

https://doi.org/10.1021/acsomega.2c05179
ACS Omega 2022, 7, 41370−41391

Table 3. Detection of Nitroaromatic Compounds by Numerous Known Methods by Employing Chemical Sensors

sensing method	materials	detection of NACs	K_{sv} (M^{-1})	LOD	reference
fluorescence method	coordination polymers $\{[Ln_2(NSBPDC)_3(H_2O)_4]\cdot x(H_2O)\}_n$ (Ln = Eu and Tb),	*p*-NT	3.93×10^3	2.5 ppm (18.57 μM)	125
fluorescence method	TPE@γ-CD-MOF-K complex	*p*-NT	2.27×10^3	3.1 ppm (22.605 μM)	126
fluorescence method	Tb-MOFs	PA	7.47×10^4		127
fluorescence method	$[CH_3\text{-dpb}]_2[Mg_3(1,4\text{-NDC})_4(\mu\ H_2O)_2(CH_3OH)(H_2O)]\cdot 1.5H_2O$	2,4-DNA	2.8×10^4 0.8×10^4		128
fluorescence method	serine-functionalized $NaYF_4:Ce^{3+}/Gd^{3+}/Eu^{3+}$ @$NaGdF_4:Tb^{3+}$	*p*-NT	0.824×10^4	6.36 ppm (46.38 μM)	129
fluorescence method	PEI-$NaCeF_4:Tb^{3+}//Eu^{3+}$	*p*-NT	0.88×10^5	5.59 ppm (40.76 μM)	130
fluorescence method	$\{[Tb(2,5\text{-TDC})_{1.5}(1,10\text{-Phen})(H_2O)]\cdot DMF\}$	*p*-NT	4.3×10^4	0.88 ppm (6.417 μM)	present work

detection, 0.88 ppm, which clearly depicts the very high sensitivity of CP **4** toward *p*-NT. As shown in Table 3, the calculated K_{sv} and LOD values for the corresponding toxic nitroanalytes are higher than those of previously reported methods.

Plausible Mechanism. The sensing of nitroaromatic compounds using Tb(III)-based CP takes place in a turn-off manner. The luminescence effect can be attributed to the photoinduced energy transfer from the ligand acting as an antenna to terbium metal ions, when excited to a particular wavelength.[41] Three mechanisms may be considered for quenching of the luminescence intensity of CP **4** in the presence of nitroanalytes (*p*-NT);

(1) From the UV−visible studies, the UV−vis absorption spectra of solutions of different nitroaromatics are investigated. It is confirmed that there is complete overlapping between the spectrum of CP **6** and the absorption spectra of *p*-NT as shown in Figure S37, so there exists competitive absorption of excitation wavelength energy between CP **4** and *p*-NT. Thus, the energy transferred by the carboxylate ligand to the Tb^{3+} ion gets reduced, which results in the significant luminescence quenching of CP **4**.[131]

(2) There may exist $\pi-\pi$ stacking interactions between the electron-deficient *p*-NT, which serves as an electron acceptor and withdraws electrons from CP **4**, and the electron-rich framework of CP **4** (electron donor). This restricts the transfer of energy/electrons from the ligand (carboxylate group of 2,5-TDC) to metal (Tb^{3+}). Therefore, the photoinduced energy/electron is transfered from the carboxylate group of the 2,5-TDC ligand to the *p*-NT and results in the fluorescence quenching behavior.[120]

(3) All the particles of CPs are able to disperse well in the nitroanalyte solutions when being dispersed. Therefore, most part of the excitation energy is absorbed by the surface of the crystals and is unable to reach the inner crystals completely. Thus, significant electron transfer occurs from the network to *p*-NT present on the surface of the CP particles. Here, the quenching effect takes place on the surface of the crystals. Based on all the above-mentioned possible quenching mechanisms, sensing of nitroaromatic explosives such as *p*-nitrotoluene, *m*-nitroaniline, *m*-dinitrobenzene, picric acid, *o*-nitrobenzaldehyde, *p*-nitrophenol, and *p*-nitroaniline can be explained.

CONCLUSIONS

In summary, by employing a dual-ligand strategy, we have successfully assembled 8 Ln(III) coordination polymers entangled with rigid 2,5-thiophenedicarboxylic acid and 1,10-phenanthroline. Crystallographic studies reveal that 2D CPs **1**−**3** crystallize in the triclinic $P\bar{1}$ space group, whereas 3D CPs **4**−**8** have a monoclinic $C2/c$ space group. For CPs **1** and **2**, Ln(III) centers exhibit two polyhedral geometries: bicapped trigonal prismatic and square antiprismatic around Ln1 and Ln2, respectively. On the other hand, for CPs **3**−**8**, Ln(III) centers display only one type of geometry: square antiprismatic geometry. The structure-corroborated DFT study reveals the existence of an interesting lp$-\pi/\pi-\pi/$lp$-\pi$ assembly in CPs **1**−**8**. The π-stacking mode between the phenanthroline rings is strong (−17.7 kcal/mol), and the strength of the S$\cdots\pi$ contact is around −3.2 kcal/mol. The coordination polymer **4** acts as a promising luminescent sensing probe for the detection of nitroaromatic compounds in aqueous medium via a luminescence quenching mechanism. It is noteworthy that the observed K_{sv} value for *p*-NT is 4.3×10^4 M^{-1} with a quenching efficiency of 97% at 100 ppm in aqueous medium. To the best of our knowledge, this is the highest value of quenching constant reported for *p*-NT.

ASSOCIATED CONTENT

Supporting Information

The Supporting Information is available free of charge at https://pubs.acs.org/doi/10.1021/acsomega.2c05179.

Structural information; FTIR spectra; powder X-ray studies; thermal analysis; emission spectra of CP **3** and **4**; sensing properties of CP 4 in different nitroanalytes; quenching efficiencies; excitation spectra of CP 4 and absorption spectra of nitro compounds; selected bond lengths and bond angles for CPs **1**−**8**; and Stern−Volmer constants and quenching efficiencies for different nitroanalytes (PDF)

Accession Codes

Supporting Information data CCDC 2181314 and 2181320−2181326 contain the supporting crystallographic data for Ln-CPs **1**−**8**. These data can be obtained free of charge via http://www.ccdc.cam.ac.uk/conts/retrieving.html or from the Cambridge Crystallographic Data Centre, 12 Union Road, Cambridge CB2 1EZ, U.K.; fax: (+44) 1223-336-033; or e-mail: deposit@ccdc.cam.ac.uk.

https://doi.org/10.1021/acsomega.2c05179
ACS Omega 2022, 7, 41370−41391

AUTHOR INFORMATION

Corresponding Author

Haq Nawaz Sheikh − *Department of Chemistry, University of Jammu, Jammu 180006, India;* orcid.org/0000-0002-2851-3831; Email: hnsheikh07@gmail.com

Authors

Nargis Akhter Ashashi − *Department of Chemistry, University of Jammu, Jammu 180006, India*

Zaib ul Nisa − *Department of Chemistry, University of Jammu, Jammu 180006, India*

Richa Singhaal − *Department of Chemistry, University of Jammu, Jammu 180006, India*

Charanjeet Sen − *Department of Chemistry, University of Jammu, Jammu 180006, India*

Musheer Ahmad − *Department of Applied Chemistry, Faculty of Engineering & Technology, Aligarh Muslim University, Aligarh 202002, India;* orcid.org/0000-0002-7446-0232

Antonio Frontera − *Department de Química, Universitat de Les Illes Balears, 07122 Palma de Mallorca, Baleares, Spain;* orcid.org/0000-0001-7840-2139

Complete contact information is available at: https://pubs.acs.org/10.1021/acsomega.2c05179

Notes

The authors declare no competing financial interest.

ACKNOWLEDGMENTS

The authors gratefully acknowledge the financial support from RUSA and DST-PURSE 2 for the instrumentation facilities availed. The authors would also like to acknowledge IIT Ropar for PXRD. N.A.A. is thankful to the Council of Scientific and Industrial Research New Delhi, India (reference no. 09/100(0234)/2019-EMR-I), for a SRF fellowship. Z.u.N. is thankful to the Council of Scientific and Industrial Research New Delhi, India (reference no. 09/100(0220)/2018-EMR-I), for a SRF fellowship. R.S. is thankful to the Council of Scientific and Industrial Research New Delhi, India (reference no. 09/100(0233)/2019-EMR-I), for a SRF fellowship. C.S. is thankful for the university research scholarship (reference no. RA/SA/URS-Ph.D/275/22). A.F. thanks the MICIU/AEI of Spain (project PID2020-115637GB-I00 FEDER funds).

REFERENCES

(1) He, G.; Peng, H.; Liu, T.; Yang, M.; Zhang, Y.; Fang, Y. A Novel Picric Acid Film Sensor Via Combination of the Surface Enrichment Effect of Chitosan Films and the Aggregation-induced Emission Effect of Siloles. *J. Mater. Chem.* **2009**, *19*, 7347−7353.

(2) Wollin, K. M.; Dieter, H. H. Toxicological Guidelines for Monocyclic Nitro-, Amino-and Aminonitroaromatics, Nitramines, and Nitrate Esters in Drinking Water. *Arch. Environ. Contam. Toxicol.* **2005**, *49*, 18−26.

(3) Nagarkar, S. S.; Desai, A. V.; Ghosh, S. K. A Fluorescent Metal−organic Framework for Highly Selective Detection of Nitro Explosives in the Aqueous Phase. *Chem. Commun.* **2014**, *50*, 8915−8918.

(4) Peng, Y.; Zhang, A. J.; Dong, M.; Wang, Y. W. A Colorimetric and Fluorescent Chemosensor for the Detection of an Explosive—2,4,6-trinitrophenol (TNP). *Chem. Commun.* **2011**, *47*, 4505−4507.

(5) Venkatramaiah, N.; Kumar, S.; Patil, S. Fluoranthene Based Fluorescent Chemo-Sensors for Detection of Explosive Nitro-aromatics. *Chem. Commun.* **2012**, *48*, 5007−5009.

(6) Dong, M.; Wang, Y. W.; Zhang, A. J.; Peng, Y. Colorimetric and Fluorescent Chemo-sensors for the Detection of 2,4,6-Trinitrophenol and Investigation of their Co-Crystal Structures. *Chem.—Asian J.* **2013**, *8*, 1321−1330.

(7) Fu, Z. H.; Wang, Y. W.; Peng, Y. Two Fluorescein-based Chemo-sensors for the Fast Detection of 2,4,6-trinitrophenol (TNP) in Water. *Chem. Commun.* **2017**, *53*, 10524−10527.

(8) Hu, Z.; Deibert, B. J.; Li, J. Luminescent Metal−organic Frameworks for Chemical Sensing and Explosive Detection. *Chem. Soc. Rev.* **2014**, *43*, 5815−5840.

(9) Yang, J. S.; Swager, T. M. Fluorescent Porous Polymer Films as TNT Chemo-sensors: Electronic and Structural Effects. *J. Am. Chem. Soc.* **1998**, *120*, 11864−11873.

(10) Halder, S.; Ghosh, P.; Hazra, A.; Banerjee, P.; Roy, P. A Quinoline-based Compound for Explosive 2, 4, 6-trinitrophenol Sensing: Experimental and DFT-D3 studies. *New J. Chem.* **2018**, *42*, 8408−8414.

(11) Wang, H.; Yuan, X.; Wu, Y.; Zeng, G.; Chen, X.; Leng, L.; Wu, Z.; Jiang, L.; Li, H. Facile Synthesis of Amino-functionalized Titanium Metal-organic Frameworks and their Superior Visible-light Photocatalytic Activity for Cr(VI) Reduction. *J. Hazard. Mater.* **2015**, *286*, 187−194.

(12) Darakas, E.; Tsiridis, V.; Petala, M.; Kungolos, A. Hexavalent Chromium Release from Lignite Fly Ash and Related Eco-toxic Effects. *J. Environ. Sci. Health, Part A: Environ. Sci. Eng.* **2013**, *48*, 1390−1398.

(13) Č≐nas, N.; Nemeikait≐-Č≐nien≐, A.; Sergedien≐, E.; Nivinskas, H.; Anusevičius, Ž.; Šarlauskas, J. Quantitative Structure−activity Relationships in Enzymatic Single-electron Reduction of Nitroaromatic Explosives: Implications for Their Cytotoxicity. *Biochim. Biophys. Acta, Gen. Subj.* **2001**, *1528*, 31−38.

(14) Schmitt, H.; Altenburger, R.; Jastorff, B.; Schüürmann, G. Quantitative Structure−activity Analysis of the Algae Toxicity of Nitroaromatic Compounds. *Chem. Res. Toxicol.* **2000**, *13*, 441−450.

(15) Ghorai, P.; Dey, A.; Hazra, A.; Dutta, B.; Brandão, P.; Ray, P. P.; Banerjee, P.; Saha, A. Cd(II) Based Coordination Polymer Series: Fascinating Structures, Efficient Semiconductors, and Promising Nitro Aromatic Sensing. *Cryst. Growth Des.* **2019**, *19*, 6431−6447.

(16) Chen, B.; Xiang, S.; Qian, G. Metal−Organic Frameworks with Functional Pores for Recognition of Small Molecules. *Acc. Chem. Res.* **2010**, *43*, 1115−1124.

(17) Allendorf, M. D.; Bauer, C. A.; Bhakta, R. K.; Houk, R. J. T. Luminescent Metal−organic Frameworks. *Chem. Soc. Rev.* **2009**, *38*, 1330−1352.

(18) Moore, D. S. Instrumentation for Trace Detection of High Explosives. *Rev. Sci. Instrum.* **2004**, *75*, 2499−2512.

(19) Moore, D. S. Recent Advances in Trace Explosives Detection Instrumentation. *Sens. Imaging: Int. J.* **2007**, *8*, 9−38.

(20) Ewing, R. G.; Atkinson, D. A.; Eiceman, G. A.; Ewing, G. J. A Critical Review of Ion Mobility Spectrometry for the Detection of Explosives and Explosive related Compounds. *Talanta* **2001**, *54*, 515−529.

(21) Meaney, M. S.; McGuffin, V. L. Luminescence-based Methods for Sensing and Detection of Explosives. *Anal. Bioanal. Chem.* **2008**, *391*, 2557−2576.

(22) Germain, M. E.; Knapp, M. J. Optical Explosives Detection: From Color Changes to Fluorescence Turn-on. *Chem. Soc. Rev.* **2009**, *38*, 2543−2555.

(23) Caygill, J. S.; Davis, F.; Higson, S. P. Current Trends in Explosive Detection Techniques. *Talanta* **2012**, *88*, 14−29.

(24) Salinas, Y.; Martínez-Máñez, R.; Marcos, M. D.; Sancenón, F.; Costero, A. M.; Parra, M.; Gil, S. Optical Chemo-sensors and Reagents to Detect Explosives. *Chem. Soc. Rev.* **2012**, *41*, 1261−1296.

(25) Sun, X.; Wang, Y.; Lei, Y. Fluorescence Based Explosive Detection: From Mechanisms to Sensory Materials. *Chem. Soc. Rev.* **2015**, *44*, 8019−8061.

(26) Lefferts, M. J.; Castell, M. R. Vapour Sensing of Explosive Materials. *Anal. Methods* **2015**, *7*, 9005−9017.

(27) Zhang, C.; Che, Y.; Zhang, Z.; Yang, X.; Zang, L. Fluorescent Nanoscale Zinc(II)-Carboxylate Coordination Polymers for Explosive Sensing. *Chem. Commun.* **2011**, *47*, 2336−2338.

(28) Wang, X. L.; Qin, C.; Wu, S. X.; Shao, K. Z.; Lan, Y. Q.; Wang, S.; Zhu, D. X.; Su, Z. M.; Wang, E. B. Bottom-Up Synthesis of Porous Coordination Frameworks: Apical Substitution of a Pentanuclear Tetrahedral Precursor. *Angew. Chem., Int. Ed.* **2009**, *48*, 5291−5295.
(29) Xuan, W. M.; Zhu, C. F.; Liu, Y.; Cui, Y. Mesoporous Metal-organic Framework Materials. *Chem. Soc. Rev.* **2012**, *41*, 1677−1695.
(30) Schnobrich, J. K.; Cychosz, K. A.; Dailly, A.; Wong-Foy, A. G.; Lebel, O.; Matzger, A. J. Linker-directed Vertex Desymmetrization for the Production of Coordination Polymers with High Porosity. *J. Am. Chem. Soc.* **2010**, *132*, 13941−13948.
(31) Su, C. Y.; Goforth, A. M.; Smith, M. D.; Pellechia, P. J.; ZurLoye, H. C. Exceptionally Stable, Hollow Tubular Metal-organic Architectures: Synthesis, Characterization, and Solid-state Transformation Study. *J. Am. Chem. Soc.* **2004**, *126*, 3576−3586.
(32) He, J.-H.; Yu, J.-H.; Zhang, Y.-T.; Pan, Q.-H.; Xu, R.-R. Synthesis, Structure, and Luminescent Property of a Heterometallic Metal-organic Framework Constructed From Rod-shaped Secondary Building Blocks. *Inorg. Chem.* **2005**, *44*, 9279−9282.
(33) Yang, E.-C.; Zhao, H.-K.; Ding, B.; Wang, X.-G.; Zhao, X.-J. Four Novel Three-Dimensional Triazole-Based Zinc (II) Metal-Organic Frameworks Controlled by the Spacers of Dicarboxylate Ligands: Hydrothermal Synthesis, Crystal Structure, and Luminescence Properties. *Cryst. Growth Des.* **2007**, *7*, 2009−2015.
(34) Li, X. Y.; Shi, W. J.; Wang, X. Q.; Ma, L. N.; Hou, L.; Wang, Y. Y. Luminescence Modulation, White Light Emission, and Energy Transfer in a Family of Lanthanide Metal−organic Frameworks Based on a Planar π-conjugated Ligand. *Cryst. Growth Des.* **2017**, *17*, 4217−4224.
(35) Ma, L. N.; Liu, Y.; Li, Y. Z.; Hu, Q. X.; Hou, L.; Wang, Y. Y. Three Lanthanide Metal-Organic Frameworks Based on an Ether-Decorated Polycarboxylic Acid Linker: Luminescence Modulation, CO_2 Capture and Conversion Properties. *Chem.—Asian J.* **2020**, *15*, 191−197.
(36) Zheng, Y. Z.; Zheng, Z.; Chen, X. M. A Symbol Approach for Classification of Molecule-based Magnetic Materials Exemplified by Coordination Polymers of Metal Carboxylates. *Coord. Chem. Rev.* **2014**, *258*−*259*, 1−15.
(37) Wang, Y. L.; Han, C. B.; Zhang, Y. Q.; Liu, Q. Y.; Liu, C. M.; Yin, S. G. Fine-tuning Ligand to Modulate the Magnetic Anisotropy in a Carboxylate-bridged Dy_2Single-Molecule Magnet System. *Inorg. Chem.* **2016**, *55*, 5578−5584.
(38) Li, R. P.; Liu, Q. Y.; Wang, Y. L.; Liu, C. M.; Liu, S. J. Evolution from Linear Tetranuclear Clusters into One-dimensional Chains of Dy(III) Single-molecule Magnets with an Enhanced Energy Barrier. *Inorg. Chem. Front.* **2017**, *4*, 1149−1156.
(39) Gong, Y. N.; Wei, X. W.; Deng, J. H.; Zhong, D. C.; Pan, C. Y. Photochromism, Photoluminescence Modulation and Selective Recognition of Small Molecules of Two Highly Stable Dynamic Metal-organic Frameworks. *Dalton Trans.* **2017**, *46*, 15656−15660.
(40) Liu, Q. Y.; Li, Y. L.; Xiong, W. L.; Wang, Y. L.; Luo, F.; Liu, C. M.; Chen, L. L. Urothermal Synthesis of Mononuclear Lanthanide Compounds: Slow Magnetization Relaxation Observed in Dy Analogue. *CrystEngComm* **2014**, *16*, 585−590.
(41) Grancha, T.; Ferrando-Soria, J.; Castellano, M.; Julve, M.; Pasán, J.; Armentano, D.; Pardo, E. Oxamato-based Coordination Polymers: Recent Advances in Multifunctional Magnetic Materials. *Chem. Commun.* **2014**, *50*, 7569−7585.
(42) Nisa, Z.; Tashi, L.; Sen, C.; Ashashi, N. A.; Sahoo, S. C.; Sheikh, H. N. Synthesis of Eight Isostructural 2D Lanthanide Coordination Polymers Assembled by Rigid Furan-2, 5-dicarboxylic Acid and Flexible Adipic Acid as Linkers and Exploration of Luminescent Eu/Tb Polymers as Efficient and Sensitive Sensors for Nitroaromatic Compounds. *New J. Chem.* **2020**, *44*, 8125−8137.
(43) Allendorf, M. D.; Stavila, V. Crystal Engineering, Structure-function Relationships, and the Future of Metal-organic Frameworks. *CrystEngComm* **2015**, *17*, 229−246.
(44) Fang, Z.; Bueken, B.; De Vos, D. E.; Fischer, R. A. Defect-engineered Metal-organic Frameworks. *Angew. Chem. Int. Ed.* **2015**, *54*, 7234−7254.
(45) Kumar, M.; Wu, L. H.; Kariem, M.; Franconetti, A.; Sheikh, H. N.; Liu, S. J.; Sahoo, S. C.; Frontera, A. A Series of Lanthanide-Based Metal-Organic Frameworks Derived from Furan-2,5-dicarboxylate and Glutarate: Structure-Corroborated Density Functional Theory Study, Magnetocaloric Effect, Slow Relaxation of Magnetization, and Luminescent Properties. *Inorg. Chem.* **2019**, *58*, 7760−7774.
(46) Chandrasekhar, V.; Bag, P.; Colacio, E. Octanuclear $\{Ln(III)_8\}$ (Ln = Gd, Tb, Dy, Ho) Macrocyclic Complexes In A Cyclooctadiene-Like Conformation: Manifestation of Slow Relaxation of Magnetization In The Dy (III) Derivative. *Inorg. Chem.* **2013**, *52*, 4562−4570.
(47) Zhang, Y.; Zheng, J. M. Three Ln(III)-2,3,5-trichlorobenzoate Coordination Polymers (Ln = Tb, Ho and Er): Syntheses, Structures And Magnetic Properties. *Inorg. Chem. Commun.* **2015**, *59*, 21−24.
(48) Cai, S. L.; Zheng, S. R.; Wen, Z. Z.; Fan, J.; Wang, N.; Zhang, W. G. Two Types of New Three-Dimensional d−f Heterometallic Coordination Polymers Based on 2-(Pyridin-3-yl)-1 H-Imidazole-4, 5-Dicarboxylate and Oxalate Ligands: Syntheses, Structures, Luminescence and Magnetic Properties. *Cryst. Growth Des.* **2012**, *12*, 4441−4449.
(49) Cai, S. L.; Zheng, S. R.; Wen, Z. Z.; Fan, J.; Zhang, W. G. A Series of New Three-Dimensional d−f Heterometallic Coordination Polymers With Rare 10-Connected *bct* Net Topology Based on Planar Hexanuclear Heterometallic Second Building Units. *Cryst. Growth Des.* **2012**, *12*, 5737−5745.
(50) Zhang, Z. H.; Song, Y.; Okamura, T. A.; Hasegawa, Y.; Sun, W. Y.; Ueyama, N. Syntheses, Structures, Near-Infrared and Visible Luminescence and Magnetic Properties of Lanthanide-Organic Frameworks With an Imidazole-Containing Flexible Ligand. *Inorg. Chem.* **2006**, *45*, 2896−2902.
(51) Xia, J.; Zhao, B.; Wang, H. S.; Shi, W.; Ma, Y.; Song, H. B.; Cheng, P.; Liao, D. Z.; Yan, S. P. Two-and three-dimensional lanthanide complexes: Synthesis, Crystal Structures and Properties. *Inorg. Chem.* **2007**, *46*, 3450−3458.
(52) Kumar, M.; Sheikh, H. N.; Franconetti, A.; Zaręba, J. K.; Sahoo, S. C.; Frontera, A. 2, 5-Furandicarboxylic Acid as a Linker for Lanthanide Coordination Polymers: The Role of Heteroaromatic $\pi-\pi$ Stacking and Hydrogen Bonding. *New J. Chem.* **2019**, *43*, 2179−2195.
(53) Li, H. H.; Shi, W.; Xu, N.; Zhang, Z. J.; Niu, Z.; Han, T.; Cheng, P. Structural Diversity of Four Metal-Organic Frameworks Based on Linear Homo/heterotrinuclear Nodes with Furan-2,5-dicarboxylic acid: Crystal Structures and Luminescent and Magnetic Properties. *Cryst. Growth Des.* **2012**, *12*, 2602−2612.
(54) Li, H.; Niu, Z.; Han, T.; Zhang, Z.; Shi, W.; Cheng, P. A Microporous Lanthanide Metal-Organic Framework Containing Channels: Synthesis, Structure, Gas Adsorption and Magnetic Properties. *Sci. China: Chem.* **2011**, *54*, 1423−1429.
(55) Li, H. H.; Li, H.; Niu, Z.; Wang, Y. P. Structural Diversity of Two Novel Dy(III) Metal-Organic Frameworks Based on Binuclear Nodes with Furan-2,5-dicarboxylic acid: Crystal Structures and Luminescent Properties. *Inorg. Chem. Commun.* **2015**, *55*, 103−107.
(56) Wang, H.; Wen, R. M.; Hu, T. L. Two Series of Lanthanide Metal-Organic Frameworks Constructed from Crown-Ether-Like Secondary Building Units. *Eur. J. Inorg. Chem.* **2014**, *2014*, 1185−1191.
(57) Wang, H.; Liu, S. J.; Tian, D.; Jia, J. M.; Hu, T. L. Temperature-Dependent Structures of Lanthanide Metal−Organic Frameworks Based on Furan-2,5-dicarboxylate and Oxalate. *Cryst. Growth Des.* **2012**, *12*, 3263−3270.
(58) Shi, F. N.; Ananias, D.; Yang, T. H.; Rocha, J. Synthesis and Characterization of Polymorphs of Photoluminescent Eu(III)-(2,5-furandicarboxylic acid, oxalic acid) MOFs. *J. Solid State Chem.* **2013**, *204*, 321−328.
(59) Wang, Y. P.; Li, X. Y.; Li, H. H.; Zhang, H. Z.; Sun, H. Y.; Guo, Q.; Li, H.; Niu, Z. A novel 3D Nd(III) Metal-Organic Frameworks Based on Furan-2,5-dicarboxylic Acid Exhibits New Topology and Rare Near-infrared Luminescence Property. *Inorg. Chem. Commun.* **2016**, *70*, 27−30.

https://doi.org/10.1021/acsomega.2c05179
ACS Omega 2022, 7, 41370−41391

(60) Akerboom, S.; Fu, W. T.; Lutz, M.; Bouwman, E. Crystal Structure and Luminescence of Complexes of Eu(III) and Tb(III) with Furan-2,5-dicarboxylate. *Inorg. Chim. Acta* **2012**, *387*, 289−293.
(61) Shi, F. N.; Pinto, M. L.; Ananias, D.; Rocha, J. Structure, Topology, Gas Adsorption and Photoluminescence of Multifunctional Porous RE^{3+} Furan-2,5-dicarboxylate Metal Organic Frameworks. *Microporous Mesoporous Mater.* **2014**, *188*, 172−181.
(62) Li, H. H.; Niu, Z.; Chen, L.; Jiang, H. B.; Wang, Y. P.; Cheng, P. Three Luminescent Metal-Organic Frameworks Constructed From Trinuclear Zinc(II)-Clusters and Furan-2,5-dicarboxylate. *CrystEngComm* **2015**, *17*, 5101−5109.
(63) Sen, R.; Mal, D.; Brandão, P.; Ferreira, R. A.; Lin, Z. Cadmium-Furandicarboxylate Coordination Polymers Prepared with Different Types of Pyridyl Linkers: Synthesis, Divergent Dimensionalities, and Luminescence Study. *Cryst. Growth Des.* **2013**, *13*, 5272−5281.
(64) Li, Y. F.; Gao, Y.; Qin, X. L.; Xu, Y.; Gao, W. Y.; Zhang, L. Structural Diversity Through Tuning Pillar: Porous Robust $[Zn_3(FDA)_3{\cdot}bpp.H_2O]{\cdot}2H_2O$ and 3-/3-D Dual Interpenetrating $[Zn(FDA)bipy]{\cdot}2H_2O$. *Inorg. Chem. Commun.* **2012**, *25*, 86−88.
(65) Nagarkar, S. S.; Chaudhari, A. K.; Ghosh, S. K. Role of Temperature on Framework Dimensionality: Supramolecular Isomers of $Zn_3(RCOO)_8$ Based Metal Organic Frameworks. *Cryst. Growth Des.* **2012**, *12*, 572−576.
(66) Du, X.; Fan, R.; Qiang, L.; Wang, P.; Song, Y.; Xing, K.; Zheng, X.; Yang, Y. Encapsulation and Sensitization of Ln^{3+} within Indium Metal-Organic Frameworks for Ratiometric Eu^{3+} Sensing and Linear Dependence of White-Light Emission. *Cryst. Growth Des.* **2017**, *17*, 2746−2756.
(67) Kumar, M.; Kariem, M.; Sheikh, H. N.; Frontera, A.; Seth, S. K.; Jassal, A. K. A Series of 3D Lanthanide Coordination Polymers Decorated with a Rigid 3,5-pyridinedicarboxylic Acid Linker: Syntheses, Structural Diversity, DFT study, Hirshfeld surface analysis, Luminescence and Magnetic Properties. *Dalton Trans.* **2018**, *47*, 12318−12336.
(68) Ay, B.; Doğan, N.; Yildiz, E.; Kani, I. A Novel Three Dimensional Samarium (III) Coordination Polymer with an Unprecedented Coordination Mode of the 2,5-Pyridinedicarboxylic Acid Ligand: Hydrothermal Synthesis, Crystal Structure and Luminescence Property. *Polyhedron* **2015**, *88*, 176−181.
(69) Ay, B.; Yildiz, E.; Kani, İ. Two Novel Isostructural and HeterolepticNd (III) and Dy (III)-organic Frameworks Constructed by 2,5-pyridinedicarboxylic Acid and in situ Generated 2-Pyridine-carboxylic Acid: Hydrothermal Synthesis, Characterization, Photo-luminescence Properties and Heterogeneous Catalytic Activities. *Polyhedron* **2017**, *130*, 165−175.
(70) Ay, B.; Yildiz, E.; Protasiewicz, J. D.; Rheingold, A. L. Hydrothermal Synthesis, Crystal Structure and Heterogeneous Catalytic Activity of a Novel Inorganic−Organic Hybrid Complex, Possessing Infinite La−O−La linkages. *Inorg. Chim. Acta* **2013**, *399*, 208−213.
(71) Ay, B.; Yildiz, E.; Kani, İ. Novel Heteroleptic Lanthanide Organic Frameworks Containing Pyridine-2,5-dicarboxylic Acid and in Situ Generated Piperazine-2,5-dicarboxylic Acid from Piperazine: Hydrothermal Synthesis and Luminescent Properties. *J. Solid State Chem.* **2016**, *233*, 44−51.
(72) Zhou, X.; Wang, H.; Jiang, S.; Xiang, G.; Tang, X.; Luo, X.; Li, L.; Zhou, X. Multifunctional Luminescent Material Eu(III) and Tb(III) Complexes with Pyridine-3,5-Dicarboxylic Acid Linker: Crystal Structures, Tunable Emission, Energy Transfer, and Temper-ature Sensing. *Inorg. Chem.* **2019**, *58*, 3780−3788.
(73) Sun, Y.-g.; Jiang, B.; Cui, T. F.; Xiong, G.; Smet, P. F.; Ding, F.; Gao, F.; Lv, T. Y.; Eeckhout, K. V.; Poelman, D.; Verpoort, F. Solvothermal Synthesis, Crystal Structure, and Properties of Lanthanide-organic Frameworks Based on Thiophene-2,5-dicarbox-ylic Acid. *Dalton Trans.* **2011**, *40*, 11581−11590.
(74) Chen, Z.; Zuo, Y.; Li, X. H.; Wang, H.; Zhao, B.; Shi, W.; Cheng, P. Structure and Luminescent Property of Novel 2D Indium(III) and 1D Cadmium (II) Coordination Polymers Based on Thiophene-2,5-dicarboxylic Acid. *J. Mol. Struct.* **2008**, *888*, 360−365.
(75) Abourahma, H.; Bodwell, G. J.; Lu, J.; Moulton, B.; Pottie, I. R.; Walsh, R. B.; Zaworotko, M. J. Coordination Polymers From Calixarene-like $[Cu_2(dicarboxylate)_2]_4$ Building Blocks: Structural Diversity *via* Atropisomerism. *Cryst. Growth Des.* **2003**, *3*, 513−519.
(76) Demessence, A.; Rogez, G.; Welter, R.; Rabu, P. Structure and Magnetic Properties of a New Cobalt(II)-thiophenedicarboxylate Coordination Polymer Showing Unprecedented Coordination. *Inorg. Chem.* **2007**, *46*, 3423−3425.
(77) Zheng, X. F.; Li, W. Q.; Du, J.; Luo, X. Z.; Liu, M. M.; Yu, Y.; Tian, L. J. Diverse Structural Assemblies of Silver−Thiophene-2,5-dicarboxylate Coordination Complexes Contribute to Different Proton-Conducting Performances. *CrystEngComm* **2016**, *18*, 7814−7822.
(78) Xue, L. P.; Chang, X. H.; Li, S. H.; Ma, L. F.; Wang, L. Y. The Structural Diversity and Photoluminescent Properties of Cadmium Thiophenedicarboxylate Coordination Polymers. *Dalton Trans.* **2014**, *43*, 7219−7226.
(79) He, Y. P.; Tan, Y. X.; Zhang, J. Organic Cation Templated Synthesis of Three Zinc-2,5-Thiophenedicarboxylate Frameworks for Selective Gas Sorption. *Cryst. Growth Des.* **2014**, *14*, 3493−3498.
(80) Kettner, F.; Worch, C.; Moellmer, J.; Gläser, R.; Staudt, R.; Krautscheid, H. Synthesis, Crystal Structure and Catalytic Behavior of Homo-and Heteronuclear Coordination Polymers $[M(tdc)(bpy)]$ (M^{2+} = Fe^{2+}, Co^{2+}, Zn^{2+}, Cd^{2+}; tdc^{2-} = 2,5-thiophenedicarboxylate). *Inorg. Chem.* **2013**, *52*, 8738−8742.
(81) Yawer, M.; Kariem, M.; Sood, P.; Sheikh, H. N. Lanthanide-Based Entangled Coordination Polymers Connected by Thiophene-2,5-dicarboxylate: Solvothermal Syntheses, Crystal Structures, Lumi-nescence and Magnetic Properties. *CrystEngComm* **2016**, *18*, 3617−3634.
(82) Rosi, N. L.; Kim, J.; Eddaoudi, M.; Chen, B.; O'Keeffe, M.; Yaghi, O. M. Rod Packings and Metal-Organic Frameworks Constructed from Rod-Shaped Secondary Building Units. *J. Am. Chem. Soc.* **2005**, *127*, 1504−1518.
(83) Li, Z. H.; Xue, L. P.; Shan, L. L.; Zhao, B. T.; Kan, J.; Su, W. P. Hydrogen Bonded-Extended Lanthanide Coordination Polymers Decorated with 2,3-thiophenedicarboxylate and Oxalate: Synthesis, Structures, and Properties. *CrystEngComm* **2014**, *16*, 10824−10829.
(84) Wang, M. X.; Long, L. S.; Huang, R. B.; Zheng, L. S. Influence of Halide Ions on the Chirality and Luminescent Property of Ionothermally Synthesized Lanthanide-Based Metal-Organic Frame-works. *Chem. Commun.* **2011**, *47*, 9834−9836.
(85) Xu, J.; Cheng, J.; Su, W.; Hong, M. Effect of Lanthanide Contraction on Crystal Structures of Three-Dimensional Lanthanide Based Metal-Organic Frameworks with Thiophene-2,5-dicarboxylate and Oxalate. *Cryst. Growth Des.* **2011**, *11*, 2294−2301.
(86) Chen, Z.; Zhao, B.; Cheng, P.; Zhao, X. Q.; Shi, W.; Song, Y. A Purely Lanthanide-Based Complex Exhibiting Ferromagnetic Cou-pling and Slow Magnetic Relaxation Behavior. *Inorg. Chem.* **2009**, *48*, 3493−3495.
(87) Eddaoudi, M.; Kim, J.; Rosi, N.; Vodak, D.; Wachter, J.; O'Keeffe, M.; Yaghi, O. M. Systematic Design of Pore Size and Functionality in Isoreticular MOFs and Their Application in Methane Storage. *Science* **2002**, *295*, 469−472.
(88) Chun, H.; Dybtsev, D. N.; Kim, H.; Kim, K. Synthesis, X-ray Crystal Structures, and Gas Sorption Properties of Pillared Square Grid Nets Based on Paddle-Wheel Motifs: Implications for Hydrogen Storage in Porous Materials. *Chem.—Eur. J.* **2005**, *11*, 3521−3529.
(89) Tian, D.; Liu, X. J.; Chen, R. Y.; Zhang, Y. H. Syntheses, Structures, Luminescent and Magnetic Properties of Two Coordina-tion Polymers Based on a Flexible Multidentate Carboxylate Ligand. *Chin. Chem. Lett.* **2015**, *26*, 499−503.
(90) Li, H. M.; Yang, S. Y.; Wang, J. W.; Long, L. S.; Huang, R. B.; Zheng, L. S. Coordination Steric Effect of N,N-dimethylformamide, N, N-dimethylacetamide and N-methyl-2-pyrrolidone on the Assembly of Coordination Polymers. *Polyhedron* **2010**, *29*, 2851−2856.

https://doi.org/10.1021/acsomega.2c05179
ACS Omega 2022, 7, 41370−41391

(91) Yang, J.; Li, G. D.; Cao, J. J.; Yue, Q.; Li, G. H.; Chen, J. S. Structural Variation From 1D to 3D: Effects of Ligands And Solvents on the Construction of Lead (II)−Organic Coordination Polymers. *Chem.—Eur. J.* **2007**, *13*, 3248−3261.
(92) Zou, G. H.; Gao, J. Crystal Structure and Luminescent Property of a New Heterometallic Coordination Polymer Based on 1D−{Ca−$(COO)_2$−Cu−$(COO)_2$−Ca}$_n$-Chains. *Synth. React. Inorg., Met.-Org., Nano-Met. Chem.* **2016**, *46*, 1721−1724.
(93) Wang, X. P.; Han, L. L.; Lin, S. J.; Li, X. Y.; Mei, K.; Sun, D. Synthesis, Structure and Photoluminescence of Three 2D Cd(II) Coordination Polymers Based on Varied Dicarboxylate Ligand. *J. Coord. Chem.* **2016**, *69*, 286−294.
(94) Kumar, M.; Li, L. Q.; Zaręba, J. K.; Tashi, L.; Sahoo, S. C.; Nyk, M.; Liu, S. J.; Sheikh, H. N. Lanthanide Contraction in Action: Structural Variations in 13 Lanthanide(III) Thiophene-2,5-dicarboxylate Coordination Polymers (Ln = La−Lu, except Pm and Tm) Featuring Magnetocaloric Effect, Slow Magnetic Relaxation, and Luminescence-lifetime-based Thermometry. *Cryst. Growth Des.* **2020**, *20*, 6430−6452.
(95) Dolomanov, O. V.; Bourhis, L. J.; Gildea, R. J.; Howard, J. A. K.; Puschmann, H. OLEX2: A Complete Structure Solution, Refinement and Analysis Program. *J. Appl. Crystallogr.* **2009**, *42*, 339−341.
(96) Sheldrick, G. M. SHELXT − Integrated space-group and crystal-structure determination. *Acta Crystallogr., Sect. A: Found. Crystallogr.* **2008**, *64*, 112−122.
(97) Sheldrick, G. M. Crystal structure refinement with SHELXL. *Acta Crystallogr., Sect. A: Found. Adv.* **2015**, *71*, 3−8.
(98) Delley, B. From Molecules to Solids with the $DMol^3$ Approach. *J. Chem. Phys.* **2000**, *113*, 7756−7764.
(99) Delley, B. Fast Calculation of Electrostatics in Crystals and Large Molecules. *J. Phys. Chem. A* **1996**, *100*, 6107−6110.
(100) Delley, B. An All-electron Numerical Method for Solving the Local Density Functional for Polyatomic Molecules. *J. Chem. Phys.* **1990**, *92*, 508−517.
(101) Blatov, V. A.; Shevchenko, A. P.; Proserpio, D. M. Applied Topological Analysis of Crystal Structures with the Program Package ToposPro. *Cryst. Growth Des.* **2014**, *14*, 3576−3586.
(102) Brandenburg, K. *DIAMOND-Crystal and Molecular Structure Visualization*; University of Bonn: Bonn, Germany, 2010.
(103) Macrae, C. F.; Edgington, P. R.; McCabe, P.; Pidcock, E.; Shields, G. P.; Taylor, R.; Towler, M.; van de Streek, J. Mercury: Visualization and Analysis of Crystal Structures. *J. Appl. Crystallogr.* **2006**, *39*, 453−457.
(104) Frisch, M. J.; Trucks, G. W.; Schlegel, H. B.; Scuseria, G. E.; Robb, M. A.; Cheeseman, J. R.; Scalmani, G.; Barone, V.; Petersson, G. A.; Nakatsuji, H.; Li, X.; Caricato, M.; Marenich, A. V.; Bloino, J.; Janesko, B. G.; Gomperts, R.; Mennucci, B.; Hratchian, H. P.; Ortiz, J. V.; Izmaylov, A. F.; Sonnenberg, J. L.; Williams-Young, D.; Ding, F.; Lipparini, F.; Egidi, F.; Goings, J.; Peng, B.; Petrone, A.; Henderson, T.; Ranasinghe, D.; Zakrzewski, V. G.; Gao, J.; Rega, N.; Zheng, G.; Liang, W.; Hada, M.; Ehara, M.; Toyota, K.; Fukuda, R.; Hasegawa, J.; Ishida, M.; Nakajima, T.; Honda, Y.; Kitao, O.; Nakai, H.; Vreven, T.; Throssell, K.; Montgomery, J. A.; Peralta, J. E., Jr.; Ogliaro, F.; Bearpark, M. J.; Heyd, J. J.; Brothers, E. N.; Kudin, K. N.; Staroverov, V. N.; Keith, T. A.; Kobayashi, R.; Normand, J.; Raghavachari, K.; Rendell, A. P.; Burant, J. C.; Iyengar, S. S.; Tomasi, J.; Cossi, M.; Millam, J. M.; Klene, M.; Adamo, C.; Cammi, R.; Ochterski, J. W.; Martin, R. L.; Morokuma, K.; Farkas, O.; Foresman, J. B.; Fox, D. J. *Gaussian 16*, revision C.01; Gaussian, Inc.: Wallingford, CT, 2016.
(105) Grimme, S.; Antony, J.; Ehrlich, S.; Krieg, H. A Consistent and Accurate ab initio Parametrization of Density Functional Dispersion Correction (DFT-D) for the 94 Elements H-Pu. *J. Chem. Phys.* **2010**, *132*, No. 154104.
(106) Weigend, F. Accurate Coulomb-Fitting Basis Sets for H to Rn. *Phys. Chem. Chem. Phys.* **2006**, *8*, 1057−1065.
(107) Boys, S. F.; Bernardi, F. The Calculation of Small Molecular Interactions by the Differences of Separate Total Energies. Some procedures with Reduced Errors. *Mol. Phys.* **1970**, *19*, 553−566.
(108) Bader, R. F. W. A Bond Path: A Universal Indicator of Bonded Interactions. *J. Phys. Chem. A* **1998**, *102*, 7314−7323.
(109) Keith, T. A. *AIMAll*, version 13.05.06; TK Gristmill Software: Overland Park, KS, 2013.
(110) Contreras-García, J.; Johnson, E. R.; Keinan, S.; Chaudret, R.; Piquemal, J. P.; Beratan, D. N.; Yang, W. NCIPLOT: A Program for Plotting Noncovalent Interaction Regions. *J. Chem. Theory Comput.* **2011**, *7*, 625−632.
(111) Johnson, E. R.; Keinan, S.; Sánchez, P. M.; García, J. C.; Cohen, A. J.; Yang, W. Revealing Noncovalent Interactions. *J. Am. Chem. Soc.* **2010**, *132*, 6498−6506.
(112) Wang, H. S.; Zhang, K.; Wang, J.; Hu, Z.; Song, Y.; Zhang, Z.; Pana, Z. Q. Regulating the Distortion Degree of the Square Antiprism Coordination Geometry in Dy−Na Single Ion Magnets. *CrystEngComm* **2021**, *23*, 3175−3184.
(113) Zhang, L. P.; Wan, Y. H.; Jin, L. P. Hydrothermal Synthesis and Crystal Structures of Three Novel Lanthanide Coordination Polymers with Glutarate and 1, 10-Phenanthroline. *J. Mol. Struct.* **2003**, *646*, 169−178.
(114) Wan, Y.; Zhang, L.; Jin, L.; Gao, S.; Lu, S. High-Dimensional Architectures From the Self-assembly of Lanthanide Ions with Benzenedicarboxylates and 1, 10-Phenanthroline. *Inorg. Chem.* **2003**, *42*, 4985−4994.
(115) Ye, J.; Zhang, J.; Ning, G.; Tian, G.; Chen, Y.; Wang, Y. Lanthanide Coordination Polymers Constructed From Dinuclear Building Blocks: Novel Structure Evolution From One-dimensional Chains to Three-dimensional Architectures. *Cryst. Growth Des.* **2008**, *8*, 3098−3106.
(116) Wang, P.; Fan, R.; Yang, Y.; Liu, X.; Cao, W.; Yang, B. Synthesis, Crystal Structures and Properties of Lanthanide-organic Frameworks Based Benzene Carboxylates With Two/three-dimensional Structure. *J. Solid State Chem.* **2012**, *196*, 441−450.
(117) Espinosa, E.; Molins, E.; Lecomte, C. Hydrogen Bond Strengths Revealed by Topological Analyses of Experimentally Observed Electron Densities. *Chem. Phys. Lett.* **1998**, *285*, 170−173.
(118) Ashashi, N. A.; Kumar, M.; Gomila, R. M.; Frontera, A.; Sheikh, H. N.; Sahoo, S. C. Solvothermal Synthesis and Crystal Structures of Two Holmium (III)-5-Hydroxyisophthalate Entangled Coordination Polymers and Theoretical Studies on The Importance of $\pi\bullet\bullet\bullet\pi$ Stacking Interactions. *J. Mol. Struct.* **2022**, *1254*, No. 132329.
(119) Ashashi, N. A.; Kumar, M.; Nisa, Z.; Frontera, A.; Sahoo, S. C.; Sheikh, H. N. Solvothermal Self Assembly of Three Lanthanide (III)-Succinates: Crystal Structure, Topological Analysis and DFT Calculations on Water Channel. *J. Mol. Struct.* **2021**, *1245*, No. 131094.
(120) Wang, J.; Sun, W.; Chang, S.; Liu, H.; Zhang, G.; Wang, Y.; Liu, Z. A Terbium Metal−Organic Framework With Stable Luminescent Emission in a Wide pH Range that Acts as a Quantitative Detection Material for Nitroaromatics. *RSC Adv.* **2015**, *5*, 48574−48579.
(121) Feng, L.; Dong, C.; Li, M.; Li, L.; Jiang, X.; Gao, R.; Wang, R.; Zhang, L.; Ning, Z.; Gao, D.; Bi, J. Terbium-based Metal-organic Frameworks: Highly Selective and Fast Respond Sensor for Styrene Detection and Construction of Molecular Logic Gate. *J. Hazard. Mater.* **2020**, *388*, No. 121816.
(122) Nisa, Z. u.; Ashashi, N. A.; Ahmed, M.; Jassal, A. K.; Frontera, A.; Sheikh, H. N. Lanthanide Coordination Polymers Functionalized by 5-Nitroisophthalic acid: Synthesis, Structure-DFT Correlation and Photoluminescent Sensor of Cd^{2+} ion. *J. Solid State Chem.* **2022**, *312*, 123229−123245.
(123) Lo, W. S.; Zhang, J.; Wong, W. T.; Law, G. L. Highly luminescent Sm^{III} complexes with intraligand charge-transfer sensitization and the effect of solvent polarity on their luminescent properties. *Inorg. Chem.* **2015**, *54*, 3725−3727.
(124) Prusti, B.; Chakravarty, M. An electron-rich small AIEgen as a solid platform for the selective and ultrasensitive on-site visual detection of TNT in the solid, solution and vapor states. *Analyst* **2020**, *145*, 1687−1694.

https://doi.org/10.1021/acsomega.2c05179
ACS Omega 2022, 7, 41370−41391

(125) Ren, L. L.; Cui, Y. Y.; Cheng, A. L.; Gao, E. Q. Water-stable Lanthanide-based Metal-organic Frameworks for Rapid and Sensitive Detection of Nitrobenzene Derivatives. *J. Solid State Chem.* **2019**, *270*, 463−469.
(126) Qiu, Z. J.; Fan, S. T.; Xing, C. Y.; Song, M. M.; Nie, Z. J.; Xu, L.; Zhang, S. X.; Wang, L.; Zhang, S.; Li, B. J. Facile Fabrication of an AIE-active Metal−organic Framework for Sensitive Detection of Explosives in Liquid and Solid Phases. *ACS Appl. Mater. Interfaces* **2020**, *12*, 55299−55307.
(127) Cao, L. H.; Shi, F.; Zhang, W. M.; Zang, S. Q.; Mak, T. C. W. Selective Sensing of $Fe^{3+}$and Al^{3+} Ions and Detection of 2, 4, 6-Trinitrophenol by a Water Stable Terbium-Based Metal−Organic Framework. *Chem.—Eur. J.* **2015**, *21*, 15705−15712.
(128) Wu, Z. F.; Gong, L. K.; Huang, X. Y. A Mg-CP with in situ encapsulated photochromic guest as sensitive fluorescence sensor for Fe^{3+}/Cr^{3+}ions and nitro-explosives. *Inorg. Chem.* **2017**, *56*, 7397−7403.
(129) Tashi, L.; Singhaal, R.; Kumar, M.; Sheikh, H. N. A down converting serine-functionalisedNaYF_4: Ce^{3+}/Gd^{3+}/Eu^{3+}@ NaGdF_4: Tb^{3+}photoluminescent probe for chemical sensing of explosive nitroaromatic compounds. *New J. Chem.* **2020**, *44*, 19908−19923.
(130) Singhaal, R.; Tashi, L.; Nisa, Z.; Ashashi, N. A.; Sen, C.; Devi, S.; Sheikh, H. N. PEI functionalized NaCeF 4: Tb^{3+}/Eu^{3+} for photoluminescence sensing of heavy metal ions and explosive aromatic nitro compounds. *RSC Adv.* **2021**, *11*, 19333−19350.
(131) Singha, D. K.; Majee, P.; Mondal, S. K.; Mahata, P. Visible detection of explosive nitroaromatics facilitated by a large stokes shift of luminescence using europium and terbium doped yttrium based MOFs. *RSC Adv.* **2015**, *5*, 102076−102084.

https://doi.org/10.1021/acsomega.2c05179
ACS Omega 2022, 7, 41370−41391